SUPPORTING INFORMATION: AB INITIO ENHANCED SAMPLING KINETIC STUDY ON MTO ETHENE METHYLATION REACTION

Simon Bailleul[a], Karen Dedecker[a], Pieter Cnudde, Louis Vanduyfhuys, Michel Waroquier, Veronique Van Speybroeck*

Center for Molecular Modeling (CMM), Ghent University, Technologiepark 46, B-9052 Zwijnaarde, Belgium

[a] Authors contributed equally

*Corresponding author: veronique.vanspeybroeck@ugent.be

TABLE OF CONTENT

1. UNIT CELL ZSM-5

As discussed in the manuscript, a unit cell of H-ZSM-5 consisting of 96 T atoms is used, as shown in Figure S 1. In this unit cell, one silicon atom is replaced by an aluminum atom to create the Brønsted acid site (BAS). As there is no simple rule for the occupation of Al atoms on the 24 distinguishable framework T sites because it depends on the conditions of the zeolite synthesis [1], the substitutions are made based on earlier work. For this, a substitution is performed at the T12 position. [2, 3] The unit cell parameters used during the simulations depends on the used methods, as the unit cell used in the static calculations is equilibrated at 0 K, while the unit cell parameters for the dynamic simulations are obtained at 623 K. Both methods are discussed in the subsequent sections.

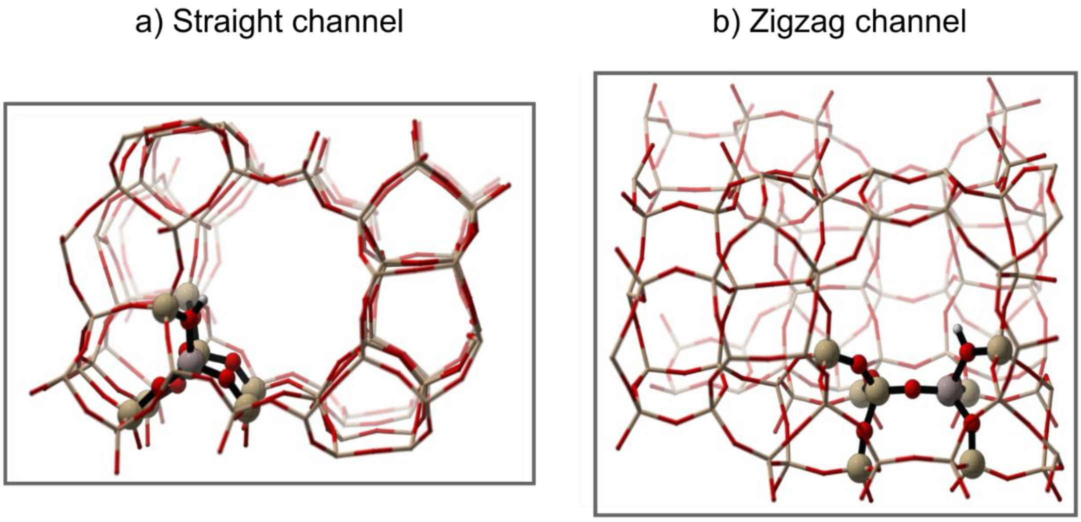

Figure S 1: H-ZSM-5 unit cell used during this study, indicating the 8T cell used during the partial Hessian vibrational analysis (PHVA).

1.1. STATIC METHOD

During all static VASP simulations, the unit cell parameters are kept constant as was done in earlier work. [4,5] Therefore, the optimal volume of the empty unit cell of H-ZSM-5 is calculated by a least square fit to the Birch Murnaghan equation of state curve of the data points depicted in Figure S 2. This led to an optimal unit cell volume of 5467.56 Å³. The used unit cell parameters are summarized in Table S 1.

.

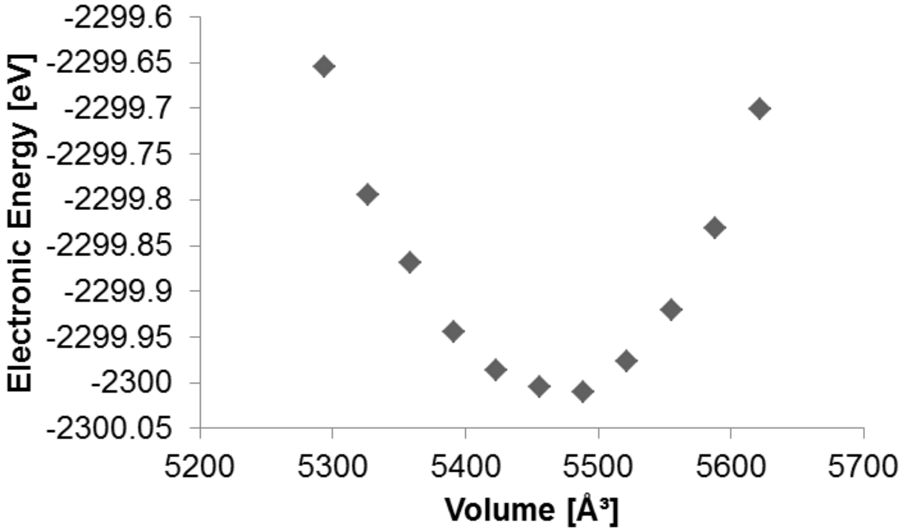

Figure S 2: Data points used for the least square fit to the Birch Murnaghan equation of state curve.[4, 5]

1.2. DYNAMIC METHOD

During dynamics simulations, the system is sampled at more realistic conditions than during the 0 K static calculations. Therefore, the unit cell parameters are averaged over a 50 ps ab initio molecular dynamics simulations in the NPT ensemble at 1 atm and 623 K, which constitutes the standard procedure employed by the authors in earlier work. [6-9] Essential is that the unit cell comprises adsorbed ethene and methanol, allowing the simulation to take fully into account the framework flexibility and the interaction with the guest molecules. The average unit cell parameters of these preliminary simulations are used for the MD production runs in the NVT ensemble.

The resulting unit cell parameters, which are used during the enhanced sampling simulations, are summarized in Table S 1.

.

Table S 1: Unit cell parameters used in the static calculations and dynamic simulations.

	a [Å]	b [Å]	c [Å]	α [°]	β [°]	γ [°]
Static	20.02	20.25	13.49	89.87	89.69	90.10
Dynamic (623 K)	20.38	20.19	13.58	90	90	90

2. CHARACTERISTIC VALUES FOR THE COLLECTIVE VARIABLES

Collective variables are expected to cover the whole transition or to be capable of identifying the transitions between metastable states in full phase space. A good set of CVs should represent a dimensionality reduction from the full space Ω to a small set of numbers. CVs should be able to describe all the relevant slow events as well as distinguish start, end and intermediate states. It is good reaction coordinate when it quantifies the dynamical progress from reactant to product.

To be a good reaction coordinate, a collective variable needs to predict distinct values for reactant, transition, product state and intermediary states, and in a good order. Throughout this paper we regard the reaction coordinate as a one-dimensional coordinate which represents progress along a reaction path. It is usually a geometric parameter that changes during the conversion of one or more molecular entities.

For each value of the reaction coordinate, there corresponds a unique configuration of all atoms giving unambiguously a snapshot of the reaction on the real reaction path. The collective variables used in this work are defined in Figure 1 of the main text. For clarity the scheme is also given in Figure S 3. Their characteristic values at the three states (reactant, transition state and product) are summarized in Table S 2. [10, 11]

Table S 2: Characteristic values of the proposed collective variables at the reactant, transition and product state.

	Reactant		Transition		Product	
	CV1	CV2	CV1	CV2	CV1	CV2
Type CN	1.0	0.0	0.5	0.5	0.0	1.0 - 2.0
Type DI	1.4 Å	5.0 Å	2.0 Å	2.4 Å	3.7 Å	1.7 Å
Type 1D-DI	3.6 Å	-	0.3 Å	-	-1.9 Å	-

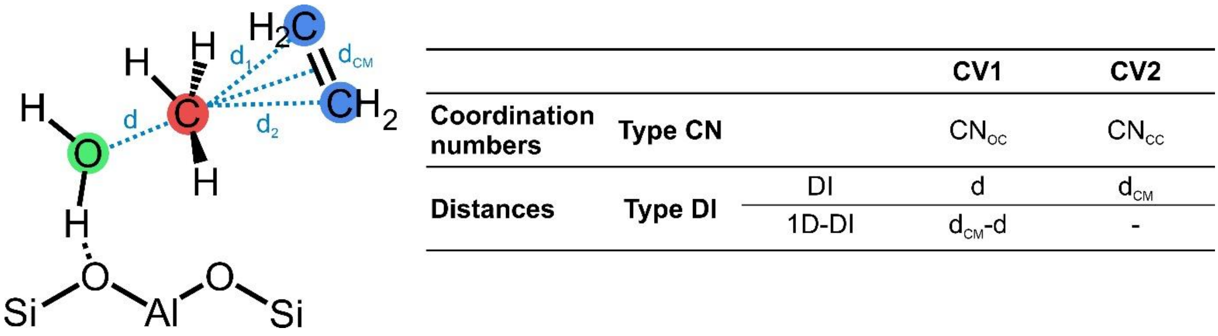

			CV1	CV2
Coordination numbers	**Type CN**		CN_{OC}	CN_{CC}
Distances	**Type DI**	DI	d	d_{CM}
		1D-DI	d_{CM}-d	-

Figure S 3: Schematic representation of the collective variables used to describe the methylation reaction of ethene. Their expected values at the reactant, transition and product state are summarized in Table S 2.

3. ENHANCED SAMPLING METHODS

In this work only a selection is made of all enhanced sampling techniques available in literature. All selected methodologies are given in Figure S 4.

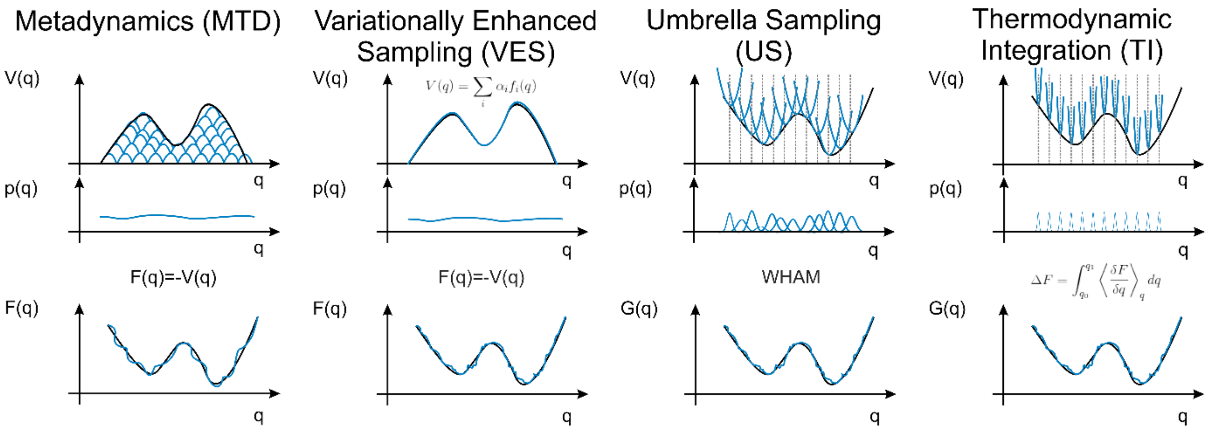

Figure S 4: Schematic representation of the enhanced sampling methodologies considered in this work, namely metadynamics (MTD), variationally enhanced sampling (VES), umbrella sampling (US) and thermodynamic integration (TI). [10]

3.1. METADYNAMICS

In this method the bias potential is constructed on the fly by gradually adding Gaussian shaped hills. The bias potential $V_G(q,t)$ becomes then the sum of all Gaussians: [12]

$$V_G(q,t) = h \sum_{\substack{t'=\tau_G, 2\tau_G, \ldots \\ t'<t}} \exp\left(-\frac{(q-q(t'))^2}{2\,w^2}\right)$$

The amplitude h and width w of the Gaussian contributions, which are added to the system after each time interval τ_G, are systematically updated during the simulation, to allow for an accurate and fast convergence. This sampling technique has first been proposed by Laio et al. [13, 14] After a sufficiently long simulation time, the bias potential is related to the free energy $F(q)$ via:

$$\lim_{t\to\infty} V_G(q,t) \sim -F(q)$$

The FES of the system can be reconstructed based on an inversion of the time dependent bias potential as displayed in Figure S 4.

Computational details of this metadynamics (MTD) technique as applied in this work are the following. We directly constructed a one-dimensional free energy surface, by selecting a 1D reaction coordinate (1D-DI in Figure S 3). The initial height of the Gaussian potentials is set to 5 kJ/mol and after each recrossing of the transition point, the height of the added Gaussian hills is adequately halved to enhance the FES convergence, until a value of 0.3125 kJ/mol was obtained. A new hill was spawned every 100 time steps. The width of all Gaussians is set to 0.04. The integration time step is set to 0.5 fs for all MTD simulations. Furthermore, quadratic walls were used to restrict the simulations to an area of interest on the FES, by limiting the diffusion of ethene and the formed water. Therefore, a quadratic upper wall is added at a value of 3.0 Å and a quadratic lower wall at -0.25 Å both with a force constant equal to 2000 kJ/(mol*Å^2). A total of 10 MTD simulations were performed, each with a sampling time between 250 and 300 ps.

3.2 VARIATIONALLY ENHANCED SAMPLING

Variationally enhanced sampling (VES) is a relatively new enhanced sampling technique introduced by Valsson and Parrinello [15] and recently applied in the construction of free energy profiles in structural transformations taking place in flexible MOFs. [10] The variational principle embedded in VES allows to introduce an arbitrary target distribution $p(q)$ that specifically targets the region we are interested in. The bias potential $V(q)$ is constructed variationally by minimizing a functional of the bias potential:

$$\Omega[V] = \frac{1}{\beta}\ln\left(\frac{\int \exp(-\beta[F(q)+V(q)])\,dq}{\int \exp\left(-\beta F(q)\right)dq}\right) + \int p(q)V(q)dq$$

It can be shown that this functional is convex with a minimum at:

$$V(q) = -F(q) - \frac{1}{\beta}\ln(p(q))$$

The free energy $F(q)$ can thus be calculated from the target distribution and the bias. An additional aspect of VES is that the minimization of the functional $\Omega[V]$ is equivalent to minimizing the Kullback-Leibler divergence between the sampled distribution p_b and the target distribution p:

$$KL\langle p|p_b\rangle = \int p(q)\ln\left(\frac{p(q)}{p_b(q)}\right)dq$$

Subsequently, the variational principle can be introduced by expanding the bias potential $V(q)$ in some basis functions $f_i(q)$, which in our work are Legendre polynomials:

$$V(q) = \sum_i \alpha_i f_i(q)$$

with expansion coefficients α_i. The expansion coefficients which minimize the functional $\Omega[V]$ can then be obtained via an efficient stochastic gradient descent algorithm. [16] Once convergence is reached, the bias potential is in a quasi-stationary state. The advantage of this method is its flexibility. There is a large flexibility in choosing the target distribution, which allows us to tailor the sampling.

In the simulations performed in this work, a uniform target distribution was chosen. Furthermore, Legendre polynomials of the 25th order are chosen as basis set. For the optimization algorithm, two parameters need to be chosen, namely the stride and step size. The stride is set to 100 steps as was done for the metadynamics simulations. The stepsize is first set to 5.0 kJ/mol and after some recrosses lowered to 1.0 kJ/mol, to have a similar procedure as in the metadynamics simulations. The same walls as in the metadynamics simulations are introduced to limit the sampling to the region of interest. A total of 5 VES simulations were performed, each with a sampling time between 300 and 350 ps.

3.3 UMBRELLA SAMPLING

In umbrella sampling (US) an external potential is added to the true Hamiltonian to enhance the sampling in low probability regions. The external potential depends on the collective variable q. The free energy $F(q)$ of the unbiased system can be obtained from the free energy of the biased system $F_b(q)$:

$$F_b(q) = F(q) + V_b(q)$$

In order to perform a decent sampling of all important regions of the configuration space, the reaction path is divided into distinct windows, as shown in Table S 3 and Figure S 4. In each window, the reaction coordinate is restrained to a target value q_i by applying a bias potential on each window. Often, a harmonic bias potential with force constant K is used to keep the system close to the target value:

$$V_i(q) = \frac{K}{2}(q - q_i)^2$$

In each window, the system mainly samples perpendicular to the collective variable. After the simulations have run, the probability distribution of all windows is combined to a total distribution function using the weighted histogram analysis (WHAM) method. [17, 18]

To create the snapshots used as a starting point for each window, a moving restrained MD simulation is used in which a bias potential is moved from one minimum to the other. Along this trajectory, 34-40 umbrellas are selected as summarized in Table S 3 (ESI) giving the location for each window. Subsequently, a restrained ab initio MD simulation of 50-60 ps is run for each umbrella to ensure sufficient sampling and overlap between the different windows. During umbrella sampling simulations, the force constants, K, are set to 1500 kJ/mol for the coordination numbers or 1500 kJ/(mol*Å^2) for the distances.

3.4 THERMODYNAMIC INTEGRATION – UMBRELLA INTEGRATION

Thermodynamic integration is actually known as umbrella integration as outlined by Kästner and Thiel [19] It is a general approach that can be regarded as a method to calculate free energy differences in constrained molecular dynamics. The constraint is imposed on the reaction coordinate q and on each point along the path $[q_0, q_1]$ the mean force is calculated being the ensemble average of the constrained MD. It contains two contributions: a force due to the potential energy and a force due to the constraint.

The free energy difference between two configurations belonging to reaction coordinates q_0 and q_1 is then given by

$$\Delta F(q_0, q_1) = \int_{q_0}^{q_1} \langle \frac{\delta F}{\delta q} \rangle_q \, dq$$

in which $-\frac{\delta F}{\delta q}$ is the force needed to maintain the reaction coordinate constraint during the simulation. The constraint is imposed during the MD by placing strong quadratic potentials.

In this work we keep the 34-40 windows along the reaction coordinate which have been introduced during the umbrella sampling simulations of type 1D-DI, but the force constant *K* is set an order of magnitude higher. Again, 50-60 ps restrained MD simulations for each window are performed over which the mean force is calculated.

4. UMBRELLA SAMPLING – WHAM

Umbrella sampling (US) is an interesting advanced sampling MD technique that is frequently used to describe an activated chemical reaction. The original concept has been proposed by Torrie and Valleau [20] in 1977 and since that time applied on countless occasions in diverse areas. Recently we also systematically made use of the US concept in constructing free-energy profiles belonging to activated chemical reactions. [7, 21, 22] Being highly parallelizable, US is a very efficient sampling method. Within the context of this paper, we give a short summary of how we proceed in enhancing low probability regions by performing the umbrella sampling concept, and how we achieved in constructing accurate free-energy profiles.

After a suitable choice of a (one-dimensional) collective variable q (reaction coordinate) the global range of q is partitioned into windows labeled i with a certain width and characterized by the value $q_i = q_0(i)$ of the reaction coordinate. An harmonic oscillator potential $V^i_{bias}(q) = \frac{1}{2}K(q-q_i)^2$ is frequently used as bias potential in each umbrella window with the minimum coinciding in $q_0(i)$. The intention is that during a MD simulation most configurations will be visited in the window.

Important ingredients in such an US are the initial configurations in the MD runs in each window. Simulation time is 50-60 ps which is a strict minimum. We can redo the MD simulations in a window many times. Each simulation yields an unbiased free energy $F^i_{unbiased}(q)$. In practice, the q-range in a window is discretized in bins. We systematically use a total number of 100 bins in each umbrella window. Here a statistical error can be extracted.

The methodology of the US technique used in the Section S 3 does not differ fundamentally from that of Zhu and Hummer [23]. The notation is slightly different but the final coupled non-linear WHAM equations are exactly the same.

An MD run in each window can be performed sampling the configurational space. This simulation generates a biased probability $p^{i}_{bias}(q)$ that covers some range in q-space centered around q_i but which extends the width of a window which is related to the distance between the centers of two subsequent h.o. potentials : ($|q_i - q_{i\pm 1}|$). The unbiased probability is then derived from the biased probability density following the relation

$$p^{i}(q) = \frac{Z^{i}_{bias}}{Z} e^{\beta V^{i}_{bias}(q)} p^{i}_{bias}(q) . \tag{4.1}$$

To construct the global unbiased probability distribution p(q), weights are assigned to each window in the WHAM ((Weighted Histogram Analysis Method):

$$p(q) = \sum_i w_i p^{i}(q) \tag{4.2}$$

with the normalization $\sum_i w_i = 1$.

Unknowns are here the weight factors w_i and the partition functions $\frac{Z^{i}_{bias}}{Z}$, which are obeying the expressions

$$\begin{aligned} \frac{Z^{i}_{bias}}{Z} &= \frac{\int e^{-\beta(H(\mathbf{r}^N,\mathbf{p}^N)+V^{i}_{bias}(Q(\mathbf{r}^N,\mathbf{p}^N))}d\mathbf{r}^N d\mathbf{p}^N}{\int e^{-\beta H(\mathbf{r}^N,\mathbf{p}^N)}d\mathbf{r}^N d\mathbf{p}^N} \\ &= \int p^{i}(q) e^{-\beta V^{i}_{bias}(q)} dq \end{aligned} \tag{4.3}$$

In each window i the density $p^{i}(q)$ yields a free-energy profile $F^{i}(q)$ following the relation $F^{i}(q) = -k_B T \ln p^{i}(q) - k_B T \ln Z$. The weights associated to each individual umbrella probability distribution cause a shift of the different energy profiles such that we finally get a smooth behavior of the global unbiased probability distribution p(q). It implies that the weights should be determined such that the variation of the unbiased probability is minimized:

$\sigma_p^2 = \mathrm{var}(p(q)) = < p(q)^2 > - < p(q) >^2$ minimal with the constraint that $\sum_i w_i = 1$.

The variance can be worked out and rewritten as :

$$\sigma_p^2 = \sum_i w_i^2 * (\frac{Z_{bias}^i}{Z})^2 e^{2\beta V_{bias}^i(q)} \mathrm{var}(p_{bias}^i(q))$$

if we assume a Poisson distribution $\mathrm{var}(p_{bias}^i(q)) = \frac{p_{bias}^i(q)}{M_i}$ with M_i the total number of snapshots in the simulation i. Minimizing the Lagrangian $L(w_i, \lambda) = \sigma_p^2(w_i) - \lambda \sum_i w_i$ yields

$$w_i = \frac{\frac{Z}{Z_{bias}^i} M_i e^{-\beta V_{bias}^i(q)}}{\sum_i \frac{Z}{Z_{bias}^i} M_i e^{-\beta V_{bias}^i(q)}} \tag{4.4}$$

Probability density in WHAM is now given by :

$$p(q) = \frac{\sum_i H_i(q)}{\sum_i \frac{Z}{Z_{bias}^i} M_i e^{-\beta V_{bias}^i(q)}} \tag{4.5}$$

$$\frac{Z_{bias}^i}{Z} = \int p(q) e^{-\beta V_{bias}^i(q)} dq \tag{4.6}$$

The unknowns w_i and $\frac{Z_{bias}^i}{Z}$ are solved iteratively from the two above equations.

These coupled nonlinear WHAM equations coincide with those published by Zhu and Hummer in ref. [23]. They are expressed in Eqs. (7) and (15) of that reference, taking into account that the normalization $1/f_i$ in that work corresponds with $\frac{Z_{bias}^{i}}{Z}$.

The choice of the total number of windows in the partitioning of the reaction coordinate range is a crucial ingredient in the US methodology. Neighboring windows should have substantial overlap. In each window i an MD simulation is performed during 50-60 ps starting from an initial configuration. These starting configurations in each umbrella window are generated by a constrained MD simulation with a moving bias potential, which moves with a constant velocity along the entire reaction path characterized by the chosen reaction coordinate. This procedure – originally introduced by Grubmuller et a. [24] but in another context - has been applied by the authors since years with success and is explained in the SI of ref. [22]. After an equilibration run of 1 ps (2000 steps of 0.5 fs) the initial structure for the first window is determined. The moving bias potential subsequently drives the system to higher values of the reaction coordinate and this during an 1.5 ps simulation (3000 MD steps). The structure and position of the reactants in the catalyst adapt systematically at the new value of the CV. About 40 snapshots are selected from this constrained MD simulations, more or less equally distributed over the remaining 3000 steps and thus the entire range of the reaction coordinate (collective variable). Those snapshots will serve as input structures for the actual umbrella sampling simulations. Specifications of the windows are given in Table S 3 of the ESI.

WINDOWS USED IN US AND TI SIMULATIONS

As discussed in the manuscript, 40 windows are used during the sampling used to obtain free energy profiles with umbrella sampling (US) and thermodynamic integration (TI). The positions of the restraints are summarized in Table S 3.

Table S 3: Positions of the restraints used during the US and TI simulation using different collective variables.

	Type CN		Type DI		Type 1D-DI
	CN_{OC}	CN_{CC}	d	d_{CM}	d_{CM}-d
window1	0.903	0.009	1.433	5.080	3.648
window2	0.902	0.018	1.442	5.051	3.610
window3	0.894	0.014	1.381	4.947	3.565
window4	0.889	0.010	1.446	4.924	3.478
window5	0.884	0.008	1.408	4.839	3.431
window6	0.890	0.013	1.536	4.881	3.346
window7	0.892	0.017	1.413	4.610	3.197
window8	0.877	0.008	1.401	4.531	3.131
window9	0.873	0.009	1.414	4.412	2.997
window10	0.830	0.009	1.390	4.360	2.971
window11	0.809	0.034	1.400	4.150	2.750
window12	0.825	0.111	1.400	4.000	2.600
window13	0.807	0.151	1.572	3.859	2.287
window14	0.807	0.205	1.500	3.650	2.150
window15	0.884	0.353	1.500	3.500	2.000
window16	0.814	0.409	1.554	3.207	1.652
window17	0.700	0.430	1.573	3.120	1.547
window18	0.653	0.453	1.564	2.836	1.272
window19	0.580	0.400	1.600	2.750	1.150
window20	0.459	0.511	1.429	2.494	1.065
window21	0.427	0.674	1.566	2.428	0.862
window22	0.389	0.733	1.765	2.413	0.648
window23	0.303	0.673	1.821	2.460	0.639

window24	0.294	0.747	1.914	2.414	0.500
window25	0.267	0.866	2.056	2.354	0.298
window26	0.176	0.903	2.109	2.137	0.029
window27	0.145	0.938	2.302	2.310	0.008
window28	0.104	1.025	2.147	2.103	-0.045
window29	0.099	1.020	2.322	2.060	-0.262
window30	0.071	1.069	2.500	2.047	-0.453
window31	0.072	1.072	2.592	1.957	-0.636
window32	0.086	1.193	2.687	1.921	-0.766
window33	0.036	1.164	2.868	1.852	-1.015
window34	0.026	1.205	2.887	1.850	-1.037
window35	n.a.	n.a.	3.064	1.832	-1.232
window36	n.a.	n.a.	3.071	1.830	-1.241
window37	n.a.	n.a.	2.971	1.727	-1.244
window38	n.a.	n.a.	3.300	1.750	-1.550
window39	n.a.	n.a.	3.471	1.770	-1.701
window40	n.a.	n.a.	3.664	1.715	-1.949

5. ENHANCED SAMPLING ERROR ESTIMATION

For all enhanced sampling methods considered in Section 3.1 of the main manuscript and Section S 3, an estimate of the error on the profile is made in the following sections. An overview of the maximum error is given in Table S 4. These errors are comparable for metadynamics and lower for umbrella sampling compared to similar work performed by the current authors. [7]

Table S 4: Error estimations for the considered enhanced sampling methods (in kJ/mol).

Method	**Maximum error**
MTD	7.48
VES	3.42
US	1.39
TI	1.94

5.1. METADYNAMICS

To estimate an error on the metadynamics simulations, 10 parallel metadynamics simulations are performed. The resulting profiles are first translated so the free energy equals 0 kJ/mol at d_{CM}-d equal to 3 Å, leading to the profiles depicted in Figure S 5. Subsequently, an average profile and standard deviation are calculated based on these 10 profiles, resulting in the data depicted in Figure 3 of the manuscript.

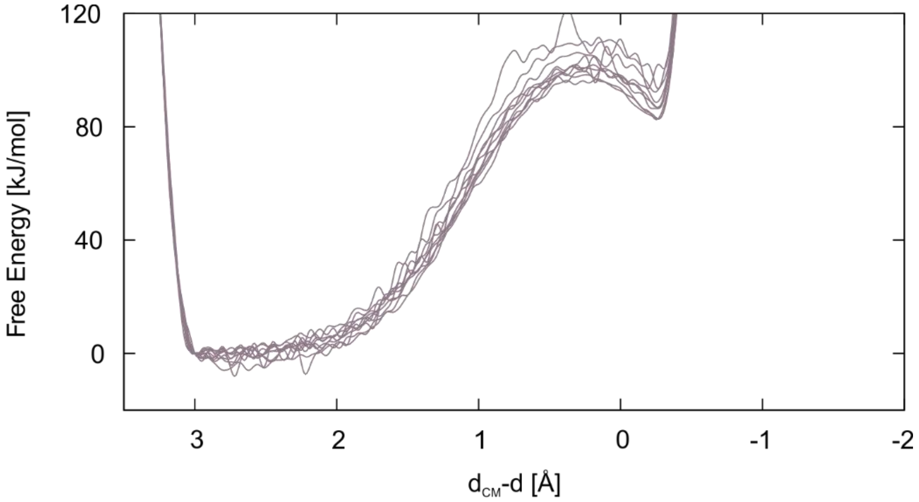

Figure S 5: Free energy profiles obtained for 10 parallel metadynamics simulations using collective variable Type 1D-DI.

5.2. VARIATIONALLY ENHANCED SAMPLING

The same methodology as for metadynamics is used to estimate the error on the variationally enhanced sampling simulations, but only 5 parallel simulations are performed. The resulting profiles are first translated so the free energy equals 0 kJ/mol at d_{CM}-d equal to 3 Å, leading to the profiles depicted in Figure S 6. Subsequently, an average profile and standard deviation are calculated based on these 5 profiles, resulting in the data depicted in Figure 3 of the manuscript.

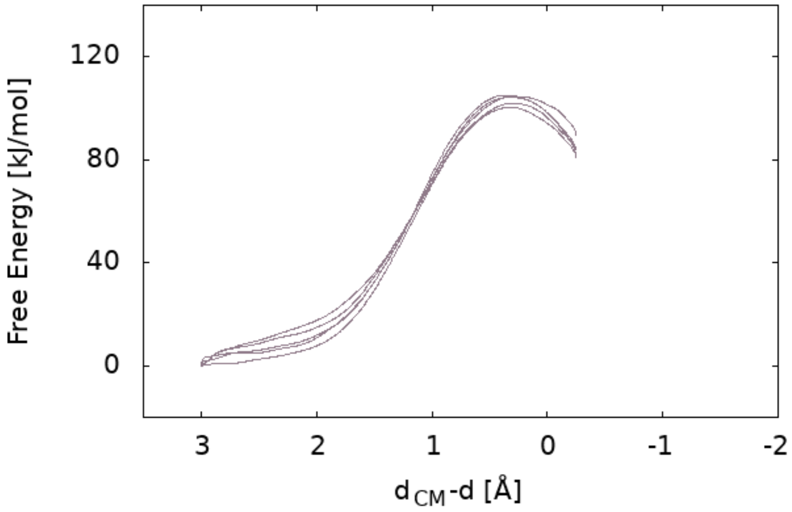

Figure S 6: Free energy profiles obtained for 5 parallel VES simulations using collective variable Type 1D-DI.

5.3. UMBRELLA SAMPLING

In the preceding Section S 3.3 a total number of 40 windows has been introduced. In each window a 50-60 ps MD simulation has been performed to obtain the density $p^i(q)$ and a free-energy profile $F^i(q)$ following the relation $F^i(q) = -k_B T \ln p^i(q) - k_B T \ln Z$. Following the WHAM methodology the global unbiased probability density can be computed by solving the coupled equations (4.5) and (4.6) of Section S 4. Knowledge of p(q) leads to the global free energy profile. Statistical error estimates can best be determined by performing several parallel simulations in each umbrella window, but this procedure is computationally extremely expensive. Therefore, we apply two algorithms which are not based on accomplishing additional simulations. The first is an efficient but rather primitive procedure: the bootstrapping method. For each window, random snapshots are selected from the original set of trajectories. The free-energy profile is recalculated. After a large number of bootstrap samples deviations at each value of q can be computed and they determine the error estimates Bootstrapping relies on random sampling with replacement. The resulting profiles are depicted in Figure S 7 .

A more established error estimation is given by Hummer [23].

By regarding the fixed position q_i in the bias h.o. potential as a variable q' , we may consider $\frac{Z^i_{bias}}{Z}$ as a state-dependent partition function : $\frac{Z^{q'}_{bias}}{Z} = \frac{Z_{bias}(q')}{Z} = \int p(q) e^{-\beta V_{bias}(q,q')} dq$ (compare with Eq. (4.6) of Sect. S 4). It delivers the total free energy $F_{bias}(q')$ in the presence of a bias potential centered at q' :

$$\begin{aligned} F_{bias}(q') &= -\frac{1}{\beta} \ln Z_{bias}(q') + \text{cte} \\ &= -\frac{1}{\beta} \ln \int p(q) e^{-\beta V_{bias}(q,q')} dq \end{aligned}$$

Following the concept of ref. [23] we may construct the mean restraining force in the simulation, by taking the derivative of $F_{bias}(q')$:

$$\frac{\partial}{\partial q'}F_{bias}(q') = \frac{K\int (q'-q)\,p(q)\,e^{-\beta V_{bias}(q,q')}dq}{\int p(q)\,e^{-\beta V_{bias}(q,q')}dq}$$

More specifically at the positions q_i , simulations have been done , and the above expression expresses the average restraining force arising from the harmonic oscillator potential centered at q_i.

$$\left.\frac{\partial}{\partial q'}F_{bias}(q')\right|_{q'=q_i} = \frac{K\int (q'-q)\,p(q)\,e^{-\beta V^{i}_{bias}(q)}dq}{\int p(q)\,e^{-\beta V^{i}_{bias}(q)}dq} = K\left\langle q_i - q\right\rangle_i = K(q_i - \left\langle q\right\rangle_i) = K(q_i - \bar{q}_i) = \bar{F}_i \qquad (5.1)$$

$\langle\rangle_i$ means the ensemble average derived from the i^{th} umbrella simulation. We also apply the shorthand notation : $\left\langle q\right\rangle_i = \bar{q}_i$ for the ensemble average.

These average forces can be computed at the h.o. centers i (i=1,S). With their knowledge free energy differences can be calculated applying the trapezoidal rule :

$$F_{bias}(q_k) - F_{bias}(q_j) = \int_{q_j}^{q_k} \left.\frac{\partial}{\partial q'}F_{bias}(q')\right|_{q'=q_i} dq_i = \frac{1}{2}\sum_{i=j}^{k-1}(\bar{F}_i + \bar{F}_{i+1})(q_{i+1} - q_i) \qquad (5.2)$$

Now it is assumed that the statistical errors in the gradient-based method are good estimates of the statistical errors in WHAM. Variances of the mean forces determine the statistical error of the biased free energies . This is an important statement. Variances of the free energy are derived from the variances of the mean forces.

From Eq. (5.1) : $\text{var}\{\bar{F}_i\} = K^2\,\text{var}\{q_i - \bar{q}_i\} = K^2\,\text{var}\{\bar{q}_i\}$ (5.3)

Choose j=1 in Eq. (5.2) and choose this state as the reference : $F_{bias}(q_1)=0$. The variance of the free energy $F_{bias}(q_k)$ can then easily be derived assuming that the average forces in each simulation are not correlated :

$$\begin{aligned} \mathrm{var}\{F_{bias}(q_k)\} = & \frac{1}{4}(q_2 - q_1)^2 K^2 \,\mathrm{var}\{\bar{q}_1\} \\ & + \frac{1}{4}(q_k - q_{k-1})^2 K^2 \,\mathrm{var}\{\bar{q}_k\} \\ & + \frac{1}{4}\sum_{i=2}^{k-1}(q_{i+1} - q_{i-1})^2 K^2 \,\mathrm{var}\{\bar{q}_i\} \end{aligned} \tag{5.4}$$

These variances in each simulation i are determined by **block averaging**. Hence $\mathrm{var}\{\bar{q}_i\}$ can be estimated without explicitly computing the autocorrelation function. Assume M_i counts (snapshots) in simulation i. Introduce n blocks and partition the snapshots of the MD simulation in these blocks (respect the sequence of appearance in the MD simulation). Define α as an index for the snapshots in a block : α = 1,m per block with $m = M_i/n$.

Average in block b : $\bar{q}_{ib} = \frac{1}{m}\sum_{\alpha=1}^{m}(q_{ib})_\alpha$

In this way we may evaluate the variance : $\mathrm{var}\{\bar{q}_i\} = \frac{1}{n(n-1)}\sum_b(\bar{q}_{ib} - \bar{q}_i)^2$.

The work of Kastner and Thiel [25, 26] should also be mentioned. Chronologically they were the first to discuss the statistical error in umbrella sampling simulations . They promote umbrella integration which provides error bars for the unbiased free energy and offer a tool to extract optimal parameters for umbrella sampling simulations. Their methodology shows some similarities with the work of Hummer [23] although some essential differences are noticed in the approach.

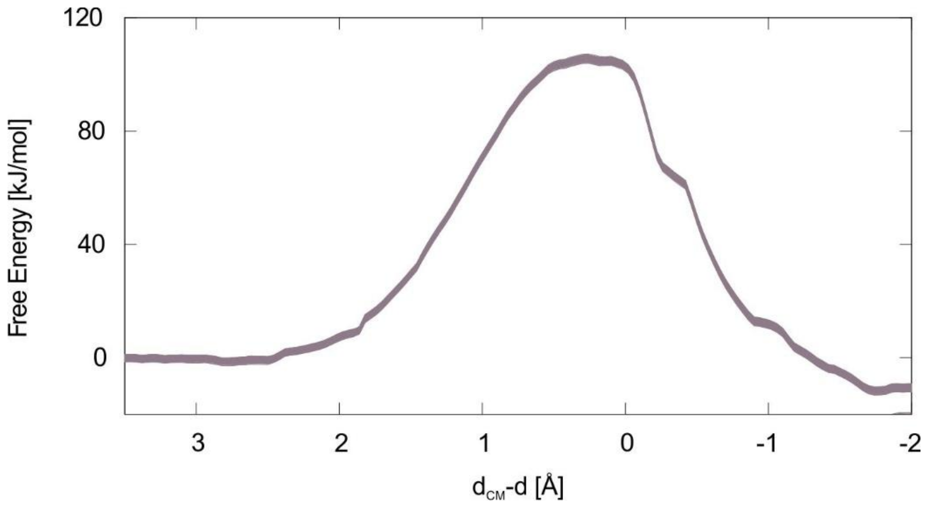

Figure S 7: Free energy profiles obtained by performing bootstrapping 100 times on the umbrella sampling simulations obtained using collective variable Type 1D-DI.

The error estimation proposed by Zhu and Hummer [23] and expressed in a concrete form (Eq. 4) leads to the accumulation of the error over the various umbrella windows, as displayed in Figure S 8.

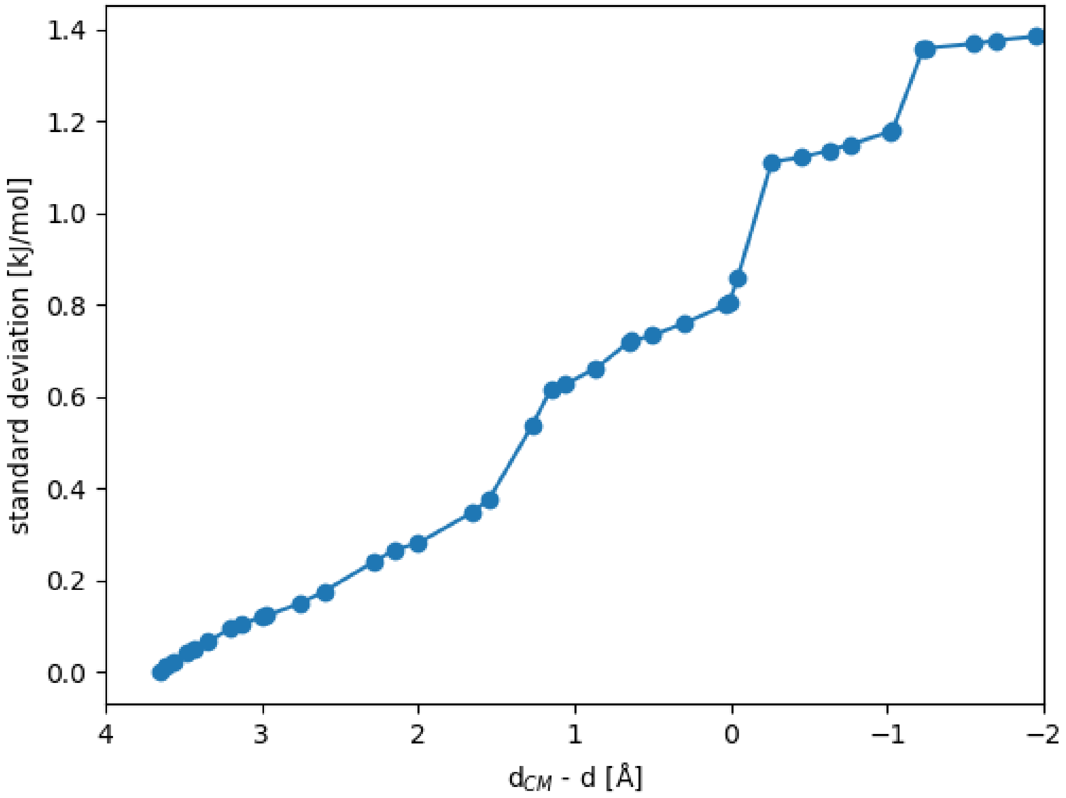

Figure S 8: Standard deviation on the free energy through block averaging on the umbrella sampling simulations obtained using collective variable Type 1D-DI.

5.4. THERMODYNAMIC INTEGRATION

Similar as for the US simulations, around 40 windows with each a 50 ps constrained MD simulation are necessary to obtain a free energy profile from thermodynamic integration simulations. Therefore, it is computationally too expensive to perform several parallel calculations for the error estimation. Instead, in first instance bootstrapping is performed to assure decent sampling. For each window, random snapshots are selected in the trajectory to obtain new 50 ps trajectories that are used to recalculate the free energy profile and corresponding error. The resulting profiles are depicted in Figure S 9.

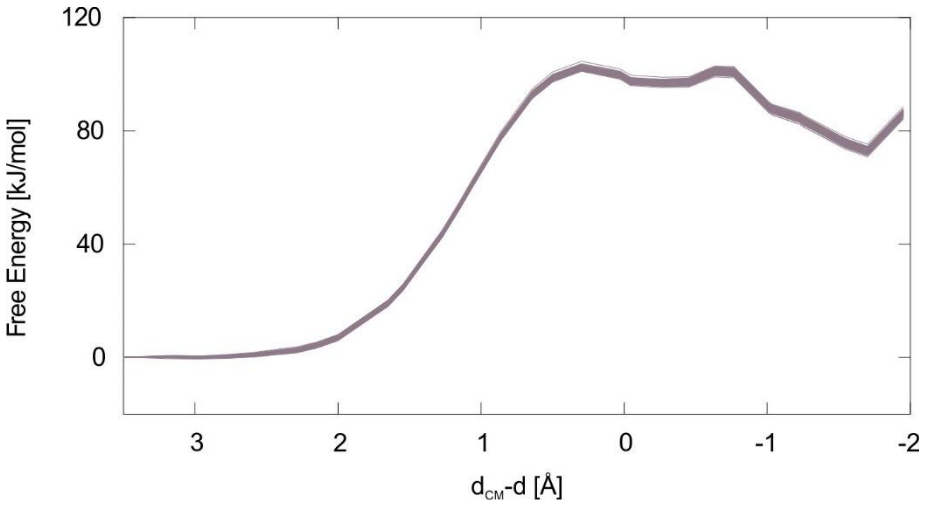

Figure S 9: Free energy profiles obtained by performing bootstrapping 100 times on the thermodynamic integration simulations obtained using collective variable Type 1D-DI.

A more reliable error estimation method as was used for the umbrella sampling simulations is employed for the thermodynamic integration simulations too. The resulting profile is depicted in Figure S 10 and clearly shows the accumulation of the error over the various windows.

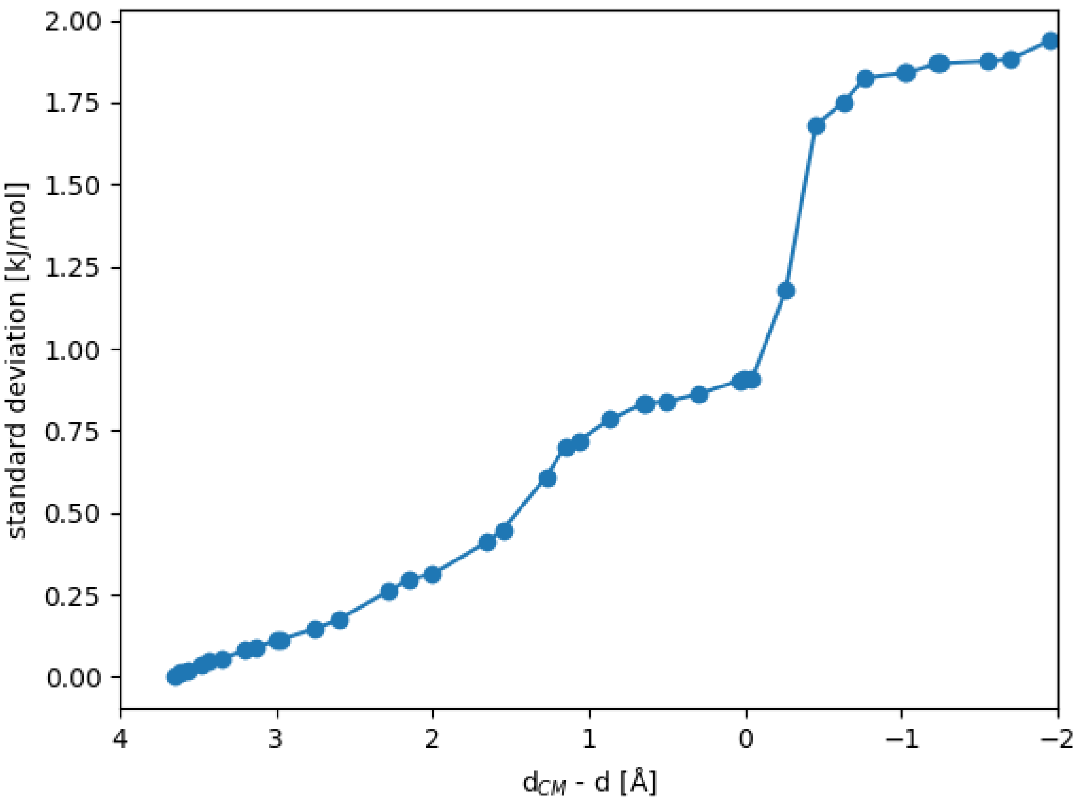

Figure S 10: Standard deviation on the free energy through block averaging on the thermodynamic integration sampling simulations obtained using collective variable Type 1D-DI.

6. PRODUCT STATE ANALYSIS US AND TI USING COLLECTIVE VARIABLE 1D-DI

As the product state of the umbrella sampling and thermodynamic integration seem to be quite different, it could be interesting to investigate the structure of the visited product states. These are summarized in Table S5. The results show that the simulations in the various umbrellas lead to the formation of different product states. Protonated propene as primary product state seems very unstable. A more detailed analysis of these product states is out of the scope of this project, as we are mainly interested in comparing the forward barrier.

Table S 5: Product state analysis of the umbrella sampling and thermodynamic integration. The positions of the windows are given in Table S 3.

	US	TI
window25	TS	TS
window26	TS	TS
window27	TS/Propoxide	TS
window28	TS/Propoxide	TS
window29	TS	TS/Primary propanol
window30	Propene	Secondary propanol
window31	Primary propanol	Secondary propanol
window32	Propoxide	Primary propanol
window33	Propoxide	Propoxide
window34	Protonated cyclopropane	Propene
window35	Cyclopropane	Propoxide
window36	Propoxide	Cyclopropane
window37	Propoxide	Propoxide
window38	Cyclopropane	Cyclopropane
window39	Cyclopropane	Propoxide
window40	Propoxide	Primary propanol

The fact that more stable products are sampled during US simulations could be ascribed to the lower force constants used in these restrained simulations. These allow US to converge to a more stable product, while the TI runs are stuck in a less stable product. This wider sampling of the CV space in US is illustrated in the histograms obtained over all windows for both methods, depicted in Figure S 11.

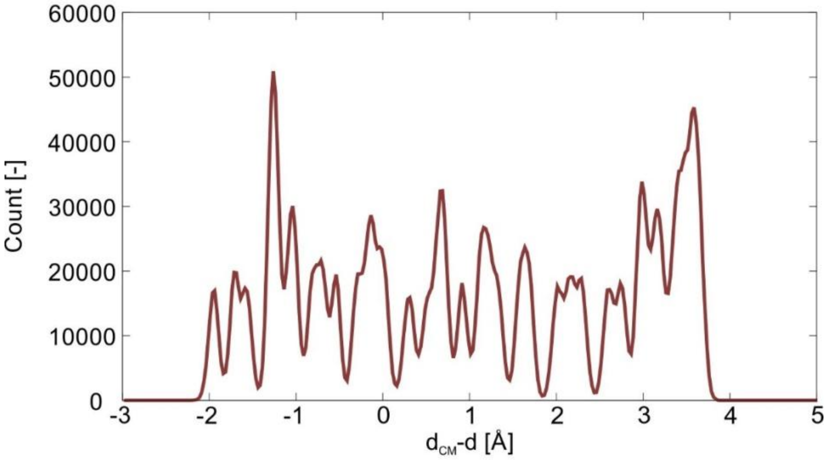

a) Umbrella Sampling

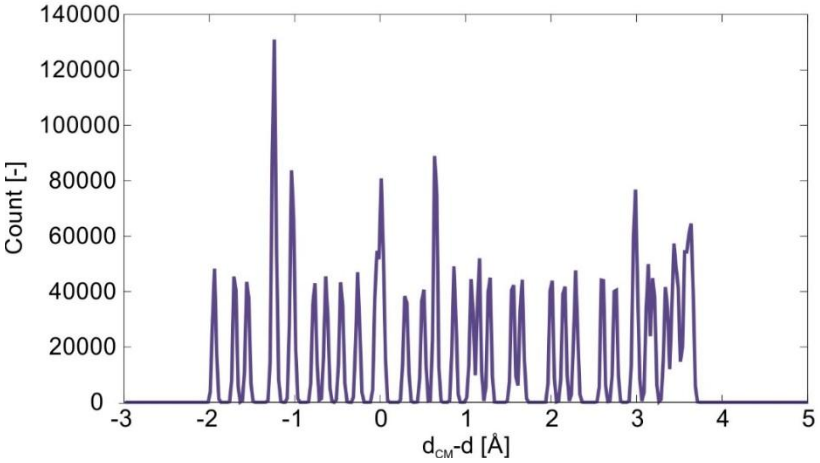

b) Thermodynamic Integration

Figure S 11: Histograms showing the collective variables sampled by combining all windows of the umbrella sampling (a) and thermodynamic integrations (b) simulations.

7. DERIVATION TRANSFORMATION FORMULA

7.1. INTRODUCTION – STATISTICAL PHYSICS

According to classical statistical mechanics, the partition function Z for an N-particle (non-identical) system and free energy F in the canonical ensemble of a system described by the Hamiltonian $H(\mathbf{r}^N,\mathbf{p}^N)=T(\mathbf{p}^N)+V(\mathbf{r}^N)$ is given by:

$$Z=\frac{1}{h^{3N}}\int e^{-\beta H(\mathbf{r}^N,\mathbf{p}^N)}d\mathbf{r}^N d\mathbf{p}^N$$

and

$$F=-k_B T\ln Z$$

We can now introduce a collective variable, i.e. a function of the coordinates describing a collective motion of the particles of the system $Q(\mathbf{r}^N)$, and further partition the partition function into contributions Z_q for fixed value of $Q(\mathbf{r}^N)=q$:

$$Z_q(q)=\frac{1}{h^{3N}}\int e^{-\beta H(\mathbf{r}^N,\mathbf{p}^N)}\,\delta(Q(\mathbf{r}^N)-q)\,d\mathbf{r}^N d\mathbf{p}^N$$

The new partition function is normalized according to :

$$\int_{-\infty}^{+\infty} Z_q(q)dq=Z$$

This also allows us to define a probability distribution p_q such that $p_q(q)dq$ represents the probability for the system to be in a state for which $Q(\mathbf{r}^N)\in[q,q+dq]$:

$$p_q(q)=\frac{Z_q(q)}{Z}$$

Through the relation between the partition function Z and the free energy F, we can relate Z_q to the free energy profile F_q:

$$F_q(q) = -k_B T \ln Z_q(q)$$

7.2. TRANSFORMATION OF 1D FREE ENERGY PROFILES

Suppose one defines two collective variables $Q_1(\mathbf{r}^N)$ and $Q_2(\mathbf{r}^N)$, which both describe the same process. This would give rise to two partition functions Z_{q1} and Z_{q2}, two probability densities p_{q1} and p_{q2} and two free energy profiles F_{q1} and F_{q2}. If both collective variables indeed describe the same process, they are expected to be correlated and the free energy profiles belonging to each of the collective variables should be related to each other. Indeed, given the free energy profile $F_{q1}(q_1)$, one can derive the free energy profile $F_{q2}(q_2)$ as follows:

$$p_{q_2}(q_2) = \int_{-\infty}^{+\infty} p_{12}(q_1, q_2) dq_1 = \int_{-\infty}^{+\infty} p_{2|1}(q_2 \mid q_1) p_{q_1}(q_1) dq_1$$

$$\frac{1}{Z} Z_{q_2}(q_2) = \int_{-\infty}^{+\infty} p_{2|1}(q_2 \mid q_1) \frac{1}{Z} Z_{q_1}(q_1) dq_1$$

$$e^{-\beta F_{q_2}(q_2)} = \int_{-\infty}^{+\infty} p_{2|1}(q_2 \mid q_1) e^{-\beta F_{q_1}(q_1)} dq_1$$

$$F_{q_2}(q_2) = -k_B T \ln\left(\int_{-\infty}^{+\infty} p_{2|1}(q_2 \mid q_1) e^{-\beta F_{q_1}(q_1)} dq_1 \right)$$

Herein, $p_{12}(q_1, q_2)$ and $p_{2|1}(q_2|q_1)$ represent the joint and conditional probability respectively. The conditional probability encodes the correlation between the two collective variables, i.e. can we predict the value of Q_2 if we know Q_1? It can be estimated from a molecular simulation by constructing histograms of the occurrence of $Q_2 = q_2$ in the subset of the simulation data for which $Q_1 = q_1$. Furthermore, it is important for this work that the conditional probability $p_{2|1}(q_2|q_1)$ can also be computed for simulations in which a bias $U_b(q_1)$ along Q_1 was applied. Relation between partition function with and without bias potential is given by: $Z_{q_1}^b(q_1) = e^{-\beta U_b(q_1)} Z_{q_1}(q_1)$ and consequently : $Z_{12}^b(q_1,q_2) = e^{-\beta U_b(q_1)} Z_{12}(q_1,q_2)$, since

$$Z_{12}(q_1,q_2) = \frac{1}{h^{3N}} \int e^{-\beta H(\mathbf{r}^N,\mathbf{p}^N)}\, \delta(Q_1(\mathbf{r}^N) - q_1)\, \delta(Q_2(\mathbf{r}^N) - q_2)\, d\mathbf{r}^N d\mathbf{p}^N$$

The conditional probability in simulations with a bias along Q_1 is readily equal to:

$$p_{2|1}^b(q_2 \mid q_1) = \frac{Z_{12}^b(q_1,q_2)}{Z_{q_1}^b(q_1)} = \frac{Z_{12}(q_1,q_2)}{Z_{q_1}(q_1)} = p_{2|1}(q_2 \mid q_1)$$

7.3. PROJECTING 2D FREE ENERGY SURFACE TO 1D FREE-ENERGY PROFILE

Assume a molecular simulation was performed that resulted in a 2D free energy surface $F_{12}(q_1, q_2)$ in terms of the collective variables $q_1 = Q_1(\mathbf{r}^N)$ and $q_2 = Q_2(\mathbf{r}^N)$. The surface can now be reduced to a one-dimensional free energy profile in terms of a reaction coordinate $q \equiv q(q_1,q_2)$, through integration of the 2D probability distribution:

$$F_q(q) = -k_B T \ln\left(\int_{-\infty}^{+\infty} \int_{-\infty}^{+\infty} e^{-\beta F_{12}(q_1,q_2)} \delta(q - q(q_1,q_2))\, dq_1\, dq_2 \right)$$

Evidently, any reduction of dimensionality implies a loss of information. In addition $q \equiv q(q_1,q_2)$ does not represent a priori a good reaction coordinate, even if q_1 and q_2 are plausible collective variables.

We illustrate this further for the case of the projection on the difference between the two collective variables $q = q_2 - q_1$:

$$
\begin{aligned}
F_q(q) &= -k_B T \ln\left(\int_{-\infty}^{+\infty} \int_{-\infty}^{+\infty} e^{-\beta F_{12}(q_1, q_2)} \delta(q - q_2 + q_1)\, dq_1\, dq_2 \right) \\
&= -k_B T \ln\left(\int_{-\infty}^{+\infty} e^{-\beta F_{12}(q_1, q_1 + q)}\, dq_1 \right)
\end{aligned}
$$

8. FREE ENERGY BARRIERS BY SUBTRACTING MINIMUM FROM MAXIMUM

As stated in the manuscript, free-energy profiles expressed in different collective variables can only be compared with each other after a relevant transformation as described in Section S 7. All the profiles obtained in this manner, depicted in Figure 6 of the main manuscript, show quite good agreement in the forward barriers after sampling in different collective variable (Q_{SAM}) spaces but transforming to the same (Q_{REP}) space.

Free-energy barriers can be easily extracted from each profile by subtracting minimum from maximum. They are all presented on the profiles displayed in Figure 5 and 6 of the main manuscript, and tabulated in Table S 6.

Table S 6: Free energy barriers (kJ/mol) for the profiles depicted in Figures 5 and 6 of the main manuscript by subtracting the minimum from the maximum.

Q_{REP} Q_{SAM}	**CN_{CC}-CN_{OC}**	**d_{CM}-d**
Type CN	127	102
Type DI	129	103
Type 1D-DI	130	107

Remark that we notice some consistency in the predicted barriers. In the space defined by the coordination numbers (Type CN), barriers amount to 127 – 130 kJ/mol, while in the space spanned by distance collective variables (Type DI) barriers are consistently lower (102 – 107 kJ/mol). It is interesting to notice that the barrier estimates are independent of the collective variable(s) in which the simulations have taken place. For both Type CN and Type DI enhanced MD simulations have been performed generating two-dimensional free-energy surfaces. They are displayed in Figure 4 of the main manuscript and in Figure S 12 of the ESI.

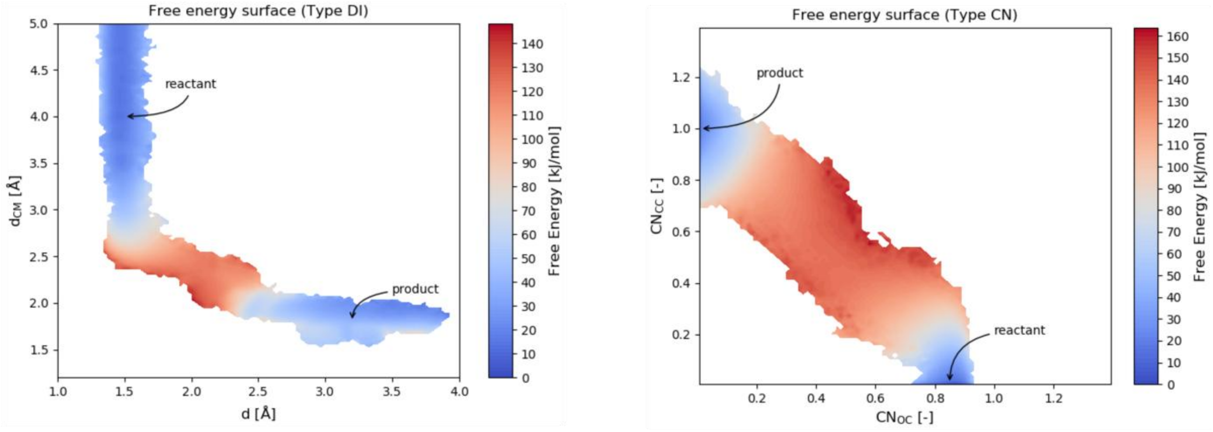

***Figure S 12** : Two-dimensional free-energy surfaces as a function of the distances d_{CM} and d (left panel), and as a function of the coordination numbers CN_{CC} and CN_{OC} as collective variables.*

To extract free-energy barriers we need to project the 2D-surfaces onto a well-chosen reaction coordinate, representing an appropriate linear combination of the two CVs. The 1D free-energy profiles are displayed in Figure 5. For the convenience of the reader and for the transparency they are also shown in Figure S 13 of the ESI.

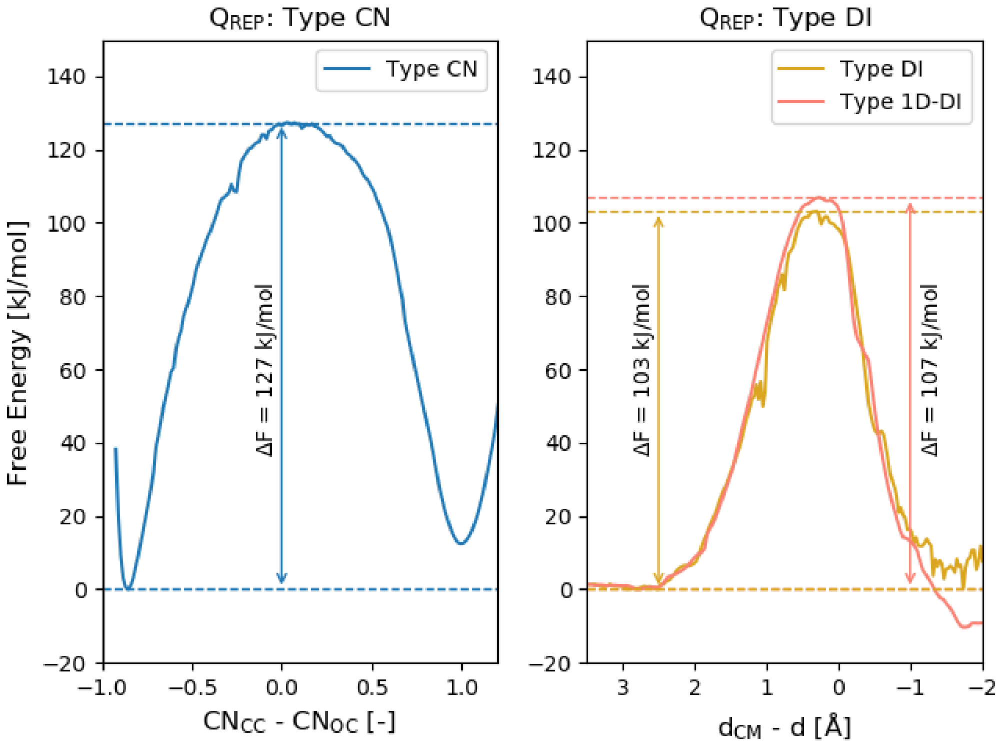

Figure S 13*: Free energy profiles at 623 K obtained by projecting the 2D-FES of Figure S 12 onto a 1D space. The left panel displays the 2D→1D reduction in the space of collective variables of Type CN (blue curve). The right panel shows the 2D→1D reduction in the space of collective variables of Type DI (yellow curve). The orange curve is the energy profile resulting from an independent sampling of the space along the one-dimensional q=d$_{CM}$ – d (1D-DI) as reaction coordinate. The forward free energy barriers are also reported on the figures.*

The free-energy profile in the one-dimensional CN$_{CC}$ – CN$_{OC}$ space shows a well-defined, thin well for the reactants. This actually corresponds with a broad range of configurations in the Type DI space. This is also represented by the mobility plots depicted in Figure S discussed in Section 10 of this ESI. The broader sampling is due to the relation between a coordination number and a distance, as can be seen in Figure S . It shows that for short and large distances, the states are projected on the values one and zero, respectively, due to the shape of the function. As the free energy relates to the probability to sample a state, the increased probability to sample the states zero and one, will lower their free energy. After the transformation to a Type DI space, we see that this corresponds to several states with similar free energy. How one can account for this configuration freedom is discussed in the main manuscript and Section 11 of this ESI.

9. DEFINITION OF A COORDINATION NUMBER

As discussed in the main manuscript, a coordination number can be used to describe the methylation of ethene. In Section 2.4.1. of the main manuscript, a coordination number is defined as:

$$CN_{ij} = \sum_{i,j} \frac{1 - \left(\frac{r_{ij}}{r_0}\right)^{nn}}{1 - \left(\frac{r_{ij}}{r_0}\right)^{nd}}$$

This is furthermore plotted for a reference distance of 2.0 Å in Figure S 14.

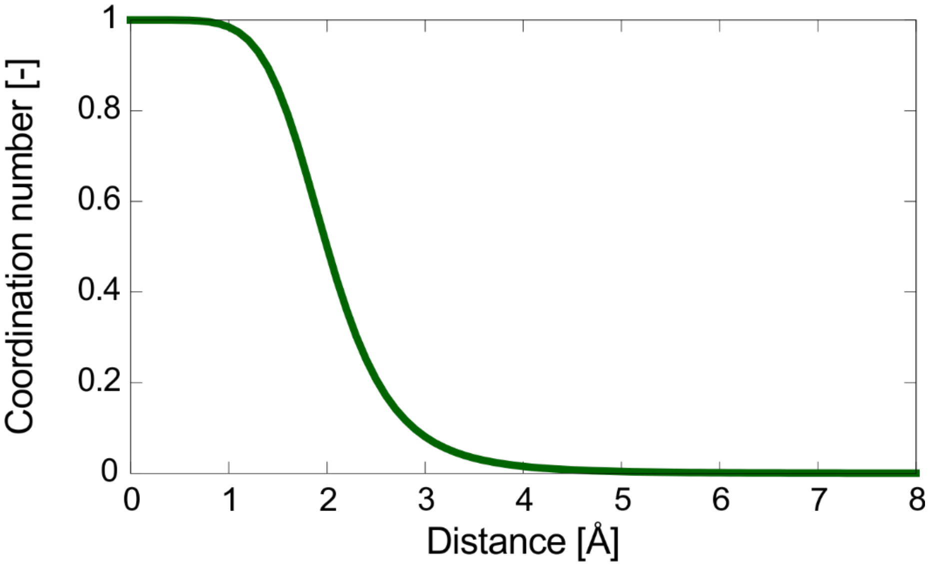

Figure S 14: *Graph showing the evolution of a coordination number with reference distance 2.0 Å in function of the distance between two atoms*

10. ANALYSIS OF THE MOBILITY OF THE REACTANTS

The free-energy profile $F(CN_{CC} - CN_{OC})$, displayed in the left panel of Figure 5 of the main manuscript, behaves differently from the free-energy profile $F(CN_{CC} - CN_{OC})$ compared with $F(d_{CM} - d)$ in the reactants basin. Window 1 (Table S 3) specifies the positions of the restraints using different CVs. They correspond to $CN_{CC} \approx 0$ and $CN_{OC} \approx 0.9$. According to the graph showing the behavior of a coordination number displayed in Figure S 14, a coordination number near zero covers a broad range of distances (3 Å – 8 Å). It implies that during a sampling in window 1 of the coordination number space the ethene molecule is allowed to migrate relatively far from the methanol. Their mutual distance is given by d_{CM}. This is confirmed by examining the mobility of the reactants during the sampling in window 1. The mobility plot is shown in Figure S 15 (b). While the methanol remains adsorbed on the Brønsted acid site, the ethene molecule diffuses almost freely through the pores. As a comparison we also perform a standard MD run without any bias (Figure S 15 (a)). We see that the situation does not vary much from the simulation with a bias potential in CN in window 1. Methanol remains in the close vicinity of the BAS while ethene also diffuses almost freely, but less accentuated than with a bias potential. An opposite result is observed when running a simulation in window 1 with a bias along a collective variable of type 1D-DI. The restraint is positioned at 3.648 Å, and it is clear that the mobility of ethene is largely restricted.

These findings undoubtedly demonstrate the different behavior observed in the reactants basin for the energy profiles in Type CN and Type DI. At increased distances, the coordination number quickly drops to 0, making all states at higher distances equivalently biased. When applying the bias on the distance on the other hand, increased distances will be subjected to an increased bias, thus limiting their sampling. Therefore, the reactant state is more broadly sampled considering Type CN as a collective variable, leading to a slightly more stabilized reactant state in the CN_{CC}-CN_{OC} free energy profile and a broader reactant state in the Type DI free energy profiles, as is clearly present in Figure 5 of the main manuscript.

.

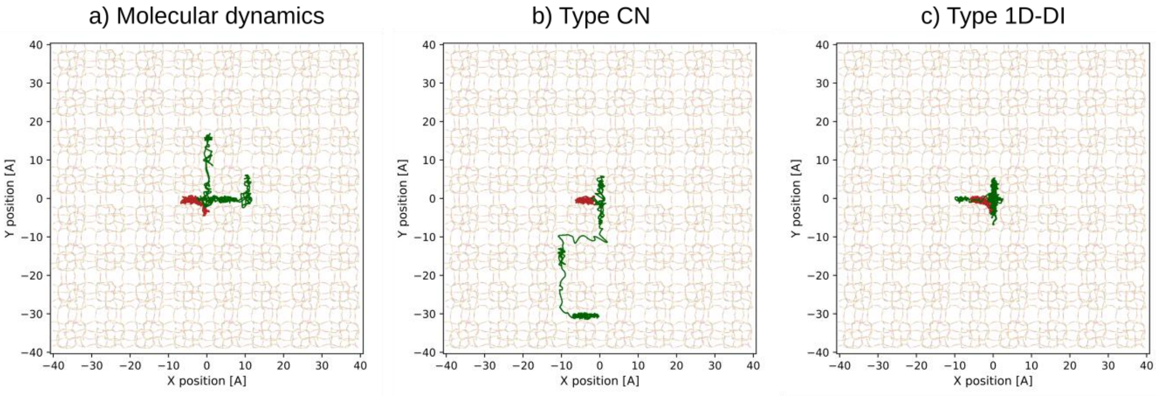

__Figure S 15:__ Mobility plots, showing the mobility of methanol (red) and ethene (green) in the reactant state for 50 ps of molecular dynamics simulation (a), 50 ps of sampling in window 1 of the umbrella sampling simulations using Type CN (b) and 50 ps of sampling in window 1 of the umbrella sampling simulations using Type 1D-DI.

11. REACTION RATE CALCULATIONS

To compute the rate constant *k* for the reaction $R \rightarrow P$, we start from the expression

$$k_{R\rightarrow P}^{TST} = \frac{\left\langle \dot{q}\,\theta(\dot{q})\,\delta(q-q^{\ddagger})\right\rangle}{\left\langle \theta(q^{\ddagger}-q)\right\rangle} \tag{1}$$

which is a standard equation in transition state theory. [27-30]

Herein, q represents the reaction coordinate and is a function of the molecular configuration $q \equiv Q(\mathbf{r}^N)$. $q^{\ddagger}$ represents the value of the reaction coordinate at the transition state. The population of the reactant is given by the step function $\theta(q^{\ddagger}-q)$ with his associated flux $\dot{\theta}(q-q^{\ddagger}) = \dot{q}\,\delta(q-q^{\ddagger})$. $\dot{q}$ represents the velocity associated to the reaction coordinate.

The average < > in Eq. (11.1) denotes an equilibrium average over the canonical probability density $p(\mathbf{r}^N,\mathbf{p}^N) = \frac{1}{h^{3N}}\frac{1}{Z}e^{-\beta H(\mathbf{r}^N,\mathbf{p}^N)}$ with the Hamiltonian $H(\mathbf{r}^N,\mathbf{p}^N) = \sum_{i=1}^{N}\frac{\mathbf{p}_i^2}{2m_i} + V(\mathbf{r}^N)$ of the global system. Z is the partition function of the N-particle system: $Z = \frac{1}{h^{3N}}\int e^{-\beta H(\mathbf{r}^N,\mathbf{p}^N)}d\mathbf{r}^N d\mathbf{p}^N$ (conform the notation of Section S 7). Summarizing, for an arbitrary function f(q) of the reaction coordinate, we have :

$$\begin{aligned}\left\langle f(q)\right\rangle &= \int f(q)\,\delta(q-Q(\mathbf{r}^N))\,p(\mathbf{r}^N,\mathbf{p}^N)\,d\mathbf{r}^N d\mathbf{p}^N \\ &= \frac{1}{h^{3N}}\frac{1}{Z}\int f(q)\,\delta(q-Q(\mathbf{r}^N))\,e^{-\beta H(\mathbf{r}^N,\mathbf{p}^N)}d\mathbf{r}^N d\mathbf{p}^N\end{aligned} \tag{2}$$

In the following we will adopt a slightly different notation for the reaction coordinate: the reaction coordinate will be written as q_1. This notation is more transparent if we need to introduce a complete coordinate transformation $\left\{\mathbf{r}^N,\mathbf{p}^N\right\} \Rightarrow \left\{q_1,q_s;\mathbf{p}_q{}^N\right\}$ with $\mathbf{q}^N$ comprising the reaction coordinate q_1 and the remaining orthogonal coordinates q_s with dimension (3N-1).

The rate constant $k_{R\to P}^{TST}$ (Eq. (11.1)) can be expressed explicitly as :

$$k_{R\to P}^{TST} = \frac{\int \dot{q}_1 \;\theta(\dot{q}_1)\delta(q_1^\ddagger - q_1(\mathbf{r}^N))e^{-\beta H(\mathbf{r}^N,\mathbf{p}^N)}d\mathbf{r}^N d\mathbf{p}^N}{\int_R e^{-\beta H(\mathbf{r}^N,\mathbf{p}^N)}d\mathbf{r}^N d\mathbf{p}^N} \tag{3}$$

where the denominator

$$\left\langle \theta(q_1^\ddagger - q_1)\right\rangle = \frac{1}{h^{3N}}\int_R e^{-\beta H(\mathbf{r}^N,\mathbf{p}^{NN})}d\mathbf{r}^N d\mathbf{p}^N$$

is the probability to find the system at the reactant side.

Integration over the velocities or momenta can be done explicitly.

(i) The most transparent way is to work in the hyperspace spanned by a complete set of generalized coordinates $\left\{q_1, q_s; \mathbf{p}_q{}^N\right\}$ where the reaction coordinate is the first coordinate of the new set. The transformation $\left\{\mathbf{r}^N, \mathbf{p}^N\right\} \Rightarrow \left\{q_1, q_s; \mathbf{p}_q{}^N\right\}$ is canonical, and in principle the q_s coordinates are arbitrary.

It should enable us to treat $\theta(\dot{q}_1)$ in a correct way:

$$k_{R\to P} = \frac{\int Zp_{q_1}\,\theta(p_{q_1})\delta(q_1^\ddagger - q_1)e^{-\beta H(q^{3N},p_q{}^{3N})}dq_1 dq_s{}^{3N-1}dp_{q_1}dp_{q_s}^{3N-1}}{\int_R e^{-\beta H(q^{3N},p_q{}^{3N})}dq^{3N}dp_q{}^{3N}} \tag{4}$$

The coordinate transformation also implies that we need to transform the kinetic energy T into the new coordinates :

$$T = \frac{1}{2}\sum_{km}\left(\sum_{i=1}^{N} m_i \sum_{\mu=x,y,z}\frac{\partial r_{i,\mu}}{\partial q_k}\frac{\partial r_{i,\mu}}{\partial q_m}\right)\dot{q}_k\dot{q}_m = \frac{1}{2}\dot{q}^T M\dot{q}$$

with the generalized mass matrix : $M_{km} = \sum_{i=1}^{N} m_i \sum_{\mu=x,y,z} \frac{\partial r_{i,\mu}}{\partial q_k} \frac{\partial r_{i,\mu}}{\partial q_m}$

(block matrix notation $M = \begin{pmatrix} M_{11} & M_{1s} \\ M_{s1} & M_s \end{pmatrix}$)

The momenta p_q associated to the generalized coordinates q are defined following

$(p_q)_k = \frac{\partial T}{\partial \dot{q}_k} = \sum_m M_{km} \dot{q}_m$ or in matrix form $p_q = M\dot{q}$. Reversely $\dot{q} = M^{-1} p_q$ and the kinetic energy is also expressed as : $T = \frac{1}{2} p_q^T M^{-1} p_q$ (5)

since M is a symmetric matrix.

The inverse matrix M^{-1} has the structure $M^{-1} = \begin{pmatrix} Z & B_{1s} \\ B_{s1} & B_s \end{pmatrix}$ (6)

Important in the reaction rate theory will be the $(M^{-1})_{11}$ component of the inverse mass matrix, and which is mostly defined as the factor Z (do not confuse with the partition function Z) :

$$Z = (M^{-1})_{11} = \sum_{i=1}^{N} \frac{1}{m_i} \sum_{\mu=x,y,z} \left(\frac{\partial q_1}{\partial r_{i,\mu}} \right)^2 \tag{7}$$

We construct the set q_s such that B_{1s} (and B_{s1}) disappears. We assume that the 3N-1 generalized coordinates q_s are orthogonal to q_1. This assumption is completely justified as the set of generalized coordinates $\{q_s\}$ is arbitrary.

Momenta integration in the denominator of Eq. (11.4) leads to:

$$\int_R e^{-\beta H(q^{3N}, p_q^{3N})} dq^{3N} dp_q^{3N} = (\frac{2\pi}{\beta})^{\frac{3N}{2}} \int_R (\det M)^{1/2} e^{-\beta V(q^{3N})} dq^{3N}$$

with $H(q^{3N}, p_q{}^{3N}) = V(q^{3N}) + \frac{1}{2} p_q^T M^{-1} p_q$

Momenta integration in the numerator of Eq. (11.4) leads to:

$$\int e^{-\beta H(q^{3N}, p_q{}^{3N})} dp_{q_s}^{3N-1} = e^{-\beta V(q^{3N})} e^{-\frac{\beta}{2} p_{q_1} Z p_{q_1}} (\frac{2\pi}{\beta})^{\frac{3N-1}{2}} (\det M_s)^{1/2}$$

We now perform the integration over momentum p_{q1} :

$$Z \int_0^\infty p_{q_1} e^{-\frac{\beta}{2} p_{q_1} Z p_{q_1}} dp_{q_1} = k_B T$$

The integration runs from 0 to +∞ due to the presence of the step function $\theta(p_{q_1})$ in Eq. (11.4).

Eq. (11.4) can now be rewritten as :

$$k_{R\to P}^{TST} = \left(\frac{k_B T}{2\pi}\right)^{1/2} \frac{\int (\det M_s)^{1/2} \delta(q_1^{\ddagger} - q_1) e^{-\beta V(q^{3N})} dq_1 dq_s{}^{3N-1}}{\int_R (\det M)^{1/2} e^{-\beta V(q^{3N})} dq^{3N}}$$

As $Det(M) = Z^{-1} Det(M_s)$ we can perform the integration over the 3N-1 generalized coordinates q_s in both numerator and denominator:

$$e^{-\beta V(q_1;q_s)} = \int (\det M_s)^{1/2} e^{-\beta V(q^{3N})} dq_s{}^{3N-1}$$

($V(q_1;q_s)$ depends parametrically on the choice of the (3N-1) generalized coordinates q_s)

and we get the final result:

$$
\begin{aligned}
k_{R\to P}^{TST} &= \left(\frac{k_BT}{2\pi}\right)^{1/2} \frac{\int \delta(q_1^{\ddagger}-q_1)\, e^{-\beta V(q_1;q_s)}dq_1}{\int_R Z^{-1/2} e^{-\beta V(q_1;q_s)}dq_1} \\
&= \left(\frac{k_BT}{2\pi}\right)^{1/2} \frac{e^{-\beta V(q_1^{\ddagger};q_s)}}{\int_R Z^{-1/2} e^{-\beta V(q_1;q_s)}dq_1} \\
&= \left(\frac{k_BT}{2\pi}\right)^{1/2} Z_{q_1=q_1^{\ddagger}}^{1/2} \left[\frac{Z_{q_1=q_1^{\ddagger}}^{-1/2}\; e^{-\beta V(q_1^{\ddagger};q_s)}}{\int_R Z^{-1/2} e^{-\beta V(q_1;q_s)}dq_1}\right]
\end{aligned}
$$

where the expression between square brackets denotes $\dfrac{\left\langle \delta(q_1^{\ddagger}-q_1)\right\rangle_r}{\left\langle \theta(q_1^{\ddagger}-q_1)\right\rangle_r}$ with the convention that the notation $\langle\ \rangle_r$ means an average over configurational coordinates only. It represents the probability $P(q_1^{\ddagger})$ of being at $q_1^{\ddagger}$, normalized by the reactant density.

The forward transition state rate constant can thus be expressed as

$$
k_{R\to P}^{TST} = \left(\frac{k_BT}{2\pi}\right)^{1/2} \frac{\left\langle Z^{1/2}\,\delta(q_1^{\ddagger}-q_1)\right\rangle_r}{\left\langle \theta(q_1^{\ddagger}-q_1)\right\rangle_r} \tag{8}
$$

which agrees with the result reported in refs. [31, 32].

In coordinate space Eq. (11.8) can be cast into :

$$
k_{R\to P}^{TST} = \sqrt{\frac{k_BT}{2\pi}}\, \frac{\int Z^{1/2}\; e^{-\beta V(\mathbf{r}^N)}\, \delta(q_1(\mathbf{r}^N)-q_1^{\ddagger})\, d\mathbf{r}^N}{\int_R e^{-\beta V(\mathbf{r}^N)} d\mathbf{r}^N} \tag{8'}
$$

(ii) An alternative way is performing a canonical transformation towards mass-weighted coordinates : $\mathbf{x}_i = \sqrt{m_i}\,\mathbf{r}_i$ and $\mathbf{P}_i = \dfrac{1}{\sqrt{m_i}}\mathbf{p}_i$. And thus :

$$
\dot{q}_1 = \sum_{j=1}^{3N} \frac{\partial q_1}{\partial x_j}\dot{x}_j = \sum_{j=1}^{3N} \frac{\partial q_1}{\partial x_j} P_j = \left|\vec{\nabla}_x q_1\right| \left|\mathbf{P}\right| \cos\vartheta
$$

$\theta(\dot{q}_1)$ implies that the angle θ varies from 0 to $\pi/2$.

$$k_{R\to P}^{TST} = \frac{\int \left|\vec{\nabla}_x q_1\right| \left|\mathbf{P}\right| \cos\vartheta \; \delta(q_1^{\ddagger} - q_1(\mathbf{x}^N)) e^{-\beta H(\mathbf{x}^N, \mathbf{P}^N)} d\mathbf{x}^N d\mathbf{P}^N}{\int_R e^{-\beta H(\mathbf{x}^N, \mathbf{P}^N)} d\mathbf{x}^N d\mathbf{P}^N}$$

After some complex analytical elaboration we get :

$$k_{R\to P}^{TST} = \sqrt{\frac{k_B T}{2\pi}} \frac{\int \left|\vec{\nabla}_{x.} q_1\right| \, e^{-\beta V(\mathbf{x}^N)} \, \delta(q_1(\mathbf{x}^N) - q_1^{\ddagger}) \, d\mathbf{x}^N}{\int_R e^{-\beta V(\mathbf{x}^N)} d\mathbf{x}^N} \tag{9}$$

We observe now that $\left|\vec{\nabla}_x q_1\right| = \left[\sum_{i=1}^{N} \sum_{\mu=x,y,z} \frac{\partial q_1}{\partial x_{i,\mu}} \frac{\partial q_1}{\partial x_{i,\mu}}\right]^{1/2} = \left[\sum_{i=1}^{N} \frac{1}{m_i} \sum_{\mu=x,y,z} \frac{\partial q}{\partial r_{i,\mu}} \frac{\partial q}{\partial r_{i,\mu}}\right]^{1/2} = Z^{1/2}$

which relates Eq. (11.9) with Eq. (11.8’).

Free energy :

As $P(q_1^{\ddagger}) = \frac{\left\langle \delta(q_1^{\ddagger} - q_1)\right\rangle_r}{\left\langle \theta(q_1^{\ddagger} - q_1)\right\rangle_r}$ represents the probability that the system is at $q_1^{\ddagger}$ normalized by the reactant density, it is convenient to introduce some reference value q_R of the reaction coordinate characteristic for the reactant state. [29] The free energy needed to shift the reaction coordinate from the value of $q_{1,R}$ to $q_1^{\ddagger}$ is then given by :

$$\Delta F_{q_{1,R}\to q_1^{\ddagger}} = -k_B T \ln\left[\frac{P(q_1^{\ddagger})}{P(q_{1,R})}\right] \tag{10}$$

The forward transition-state rate constant can be rewritten as :

$$k_{R\to P}^{TST} = \left(\frac{k_B T}{2\pi}\right)^{1/2} \left\langle Z^{1/2}\right\rangle_{q=q^{\ddagger}} P(q_R) e^{-\beta \Delta F_{q_R \to q^{\ddagger}}}$$

(coinciding with the expression reported in Bucko et al. [29]), or

$$k_{R\to P}^{TST} = A \frac{e^{-\beta \Delta F_{q_{1,R}\to q_1^{\ddagger}}}}{\int_{-\infty}^{q^{\ddagger}} e^{-\beta F(q)} dq} \tag{11}$$

with a prefactor $A = \left(\frac{k_B T}{2\pi}\right)^{1/2} \left\langle Z^{1/2}\right\rangle_{q_1 = q_1^{\ddagger}}$ (12)

$\Delta F_{q_{1,R} \to q_1^{\ddagger}}$ should be interpreted as the reversible work to bring the system from the reactant valley to the transition state. Usually, all free energy differences are relative with respect to the reference state corresponding with reaction coordinate $q_{1,R}$ which is characteristic with the reactant valley.

$$P(q_{1,R}) = \frac{\langle \delta(q_{1,R} - q_1) \rangle}{\langle \theta(q_1^{\ddagger} - q_1) \rangle}$$

is the probability density of $q_{1,R}$ within the ensemble of reactant configurations.

The computation of the term $\Delta F_{q_{1,R} \to q_1^{\ddagger}}$ can be obtained from the blue moon ensemble method [30, 32] but also from other enhanced MD techniques such like Umbrella Sampling (US), Metadynamics (MTD), etc. All free energies are regarded as relative with respect to the reference reactant state corresponding to q_R. In this work the free energy profile is computed within the Umbrella Sampling protocol and $\Delta F_{q_{1,R} \to q_1^{\ddagger}}$ is then determined by the maximum – minimum difference.

As $P(q_{1R}) = \frac{\langle \delta(q_{1R} - q_1) \rangle_r}{\langle \theta(q_1^{\ddagger} - q_1) \rangle_r} = \frac{1}{\int_{q_{1R}}^{q_1^{\ddagger}} e^{-\beta F(q)} dq}$ ($F(q_{1R})=0$ at the reference)

the rate constant can be cast into the form :

$$k_{R \to P}^{TST} = A \frac{e^{-\beta \Delta F_{q_{1R} \to q_1^{\ddagger}}}}{\int_{q_{1R}}^{q_1^{\ddagger}} e^{-\beta F(q)} dq} \tag{13}$$

Although the expression for the prefactor A indicates that a molecular simulation needs to be performed in which the system is constrained to be in the exact transition state ($q = q^{\ddagger}$), this is not necessarily required. The prefactor can also be estimated from a molecular simulation which is instead biased by a certain bias potential $U_b(q)$ (for example during Umbrella Sampling).

$$\left\langle Z^{1/2} \right\rangle_{q_1=q_1^\ddagger} = \frac{\left\langle Z^{1/2}\delta(q_1^\ddagger - q_1) \right\rangle_{V_b}}{\left\langle \delta(q_1^\ddagger - q_1) \right\rangle_{V_b}}$$

The denominator $\bar{Z}_R = \int_{q_{1R}}^{q_1^\ddagger} e^{-\beta F(q)} dq$ is proportional to the partition function of the reactant and yields information on the width and depth of the free energy profile in terms of the collective variable in the reactant region.

Phenomenological free-energy of activation $\Delta F^\ddagger$:

Next, a phenomenological free-energy of activation $\Delta F^\ddagger$ can be defined following the procedure proposed by Bucko et al. [29] making use of the Eyring-Polanyi equation [33] and the relation for the computational rate constant :

$$\Delta F^\ddagger = \Delta F_{q_{1R} \to q_1^\ddagger} + k_B T \ln\left(\frac{k_B T}{h} \frac{\left\langle Z^{1/2} \right\rangle_{q_1=q_1^\ddagger}}{P(q_{1R})} \right) \tag{14}$$

Application to methylation reaction :

We computed the rate constants according to Eq. 13, as well as the various contributions to it, for the methylation reaction. Furthermore, to investigate the influence of the choice of the collective variable, we computed the rate constant through various approaches. First, the enhanced sampling simulations were performed using the various collective variables defined in this work. This collective variable is denoted as Q_{SAM}. Second, the resulting free energy profile can be expressed in terms of this same collective variable, but it can also be transformed to a profile in terms of one of the other CVs. The collective variable used to express the free energy profile is denoted as Q_{REP}. The reference of the free energy profiles is always chosen such that the minimum in the reactant valley is set to zero, leading to the free energy differences summarized in Table S 6. Furthermore, Table S and Table S below indicate the other contributions from Eq. 13 for various combinations of Q_{SAM} and Q_{REP}.

Table S 7: Prefactor A (in units [au]/s, with [au] atomic units of the CV) figuring in the expression of the rate constant (Eq. 12).

Q_{REP} Q_{SAM}	**CN_{CC}-CN_{OC}**	**d_{CM}-d**
Type CN	$4.85\ 10^{12}$	$1.10\ 10^{13}$
Type DI	$4.77\ 10^{12}$	$1.13\ 10^{13}$
Type 1D-DI	$4.98\ 10^{12}$	$1.17\ 10^{13}$

Table S 8: Factor proportional to the partition function of the reactant $\bar{Z}_R$ (in atomic units of the CV). This factor expresses the stability of the reactant.

Q_{REP} Q_{SAM}	**CN_{CC}-CN_{OC}**	**d_{CM}-d**
Type CN	$6.50\ 10^{-2}$	$1.00\ 10^{1}$
Type DI	$6.30\ 10^{-2}$	$2.42\ 10^{0}$
Type 1D-DI	$6.83\ 10^{-2}$	$2.30\ 10^{0}$

As can be concluded from these tables, the free energy barrier is clearly dependent on the choice of the collective variable (see Table S). However, when computing the rate constants (Table 1 of the main manuscript), this dependence is to a very large extent compensated with the factors $\bar{Z}_R$ and A. The remaining differences can be assumed to be due to numerical errors. These results imply, that one cannot simply rely on the free energy barrier to make statements on how fast a reaction will occur. Instead, one needs to compute all contributions to the reaction rate consistently.

12. COMMITTOR ANALYSIS

A first test to estimate the reliability of the obtained free energy profiles consists of calculating the committor at the transition state suggested by the resulting free energy profiles, as a consideration of the entire transition path becomes too expensive using ab initio calculations. [10] A committor is the fraction, $p_P(q)$, of trajectories which are launched from a configuration with the collective variable equal to q that end up in the product state P, before visiting the reactant state R. [11] At the transition state, this should equal 0.5. The committor is calculated for the energy profiles resulting from the enhanced MD simulations with the collective variables of type CN (projected to one-dimensional CN_{CC}-CN_{CO}), since committor analyses for higher dimensional free energy surfaces are far from trivial, and 1D-DI. From the selected snapshots – obtained in the window that samples the transition region – MD simulations are started. When such a simulation enters either the reactant or product state of the system, the simulation is stopped and we say that the simulation committed to either the reactant or product state. We define these states by the bending points in the free energy profile.

For Type 1D-DI 60 snapshots with d_{CM}-d at 0.2795 Å are selected. This value corresponds to the maximum of the barrier between the reactant and product basins as displayed on the right panel of Figure 5 (orange curve). For each snapshot, 20 MD runs are performed (all with different random initial velocities) using the built-in committor analysis method of PLUMED. The calculated value of the committor is calculated to get values of 0.50, indicating that this 1D-DI variable is indeed a suitable collective variable. Furthermore, the histogram shown in Figure S 16 is clearly peaked at $p_P(q) = 0.5$, confirming the quality of the selected collective variable.

For Type CN, we select 30 snapshots with CN_{CC}-CN_{OC} at 0.028. Again, this value corresponds to the maximum of the barrier between the reactant and product basins as displayed on the left panel of Figure 5 (blue curve). For each of these snapshots, we perform

40 MD runs (in order to obtain the same total of 1200 runs as for the Type 1D-DI committor analysis). In this situation, the committor equals 0.52, implying that the coordination numbers CN_{CC} and CN_{OC}, too, are perfectly capable of correctly identifying the

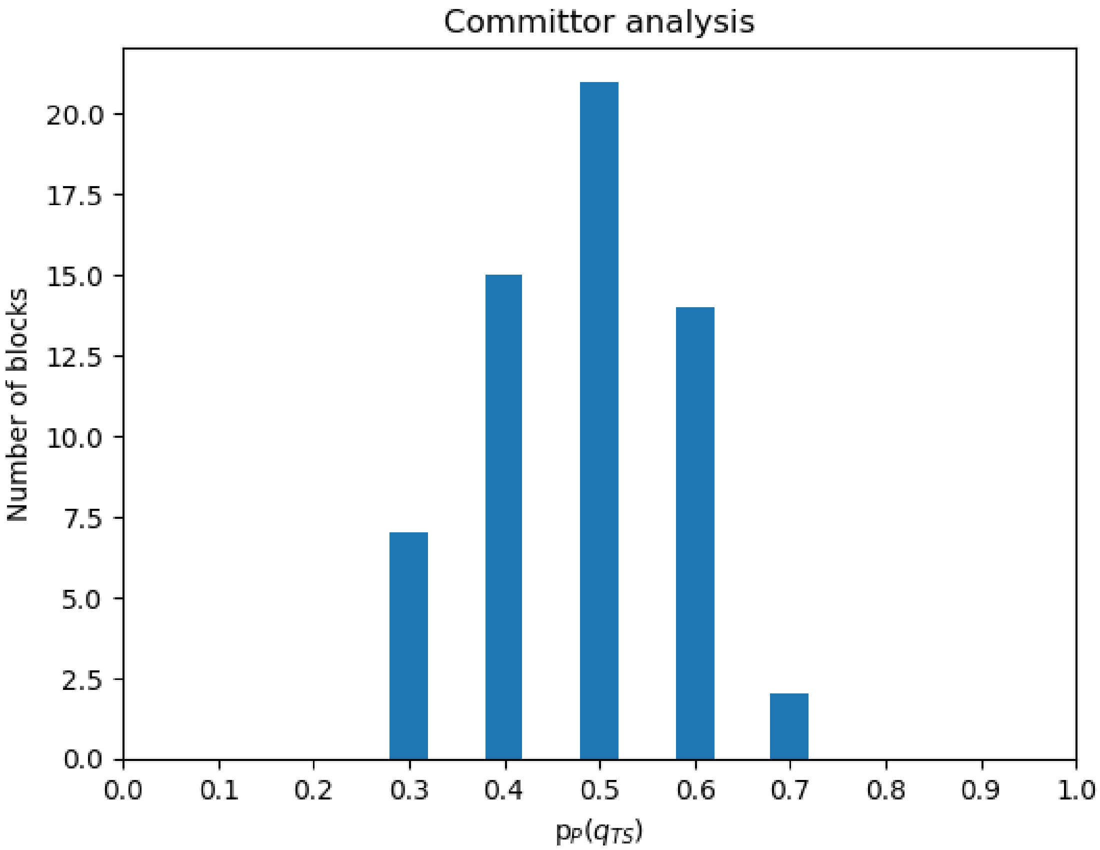

Figure S 16 : Committor histogram obtained for the transition state of CV Type 1D-DI

transition state. We also show the corresponding histogram in Figure S 17, which is also peaked near $p_P(q) = 0.5$, but with a slightly broader distribution. Note that we make a simplification in the sense that we perform the committor analysis based on a 1D projection of a 2D simulation, since we use the 1D projection to determine the value of the transition state and the boundaries of the reactant and product basins. Nevertheless, this does not affect the quality of our result, given the good value of the committor.

Systematic protocols exist to identify even better collective variables by obtaining the slowest order parameters describing the transformation from reactant to product via time-structure based independent component analysis (tICA). [34-36] Given that our collective variables are of sufficient quality, as shown by the committor analysis, and as computationally expensive MD data containing transitions are required to perform this analysis, this is out of scope of this work.

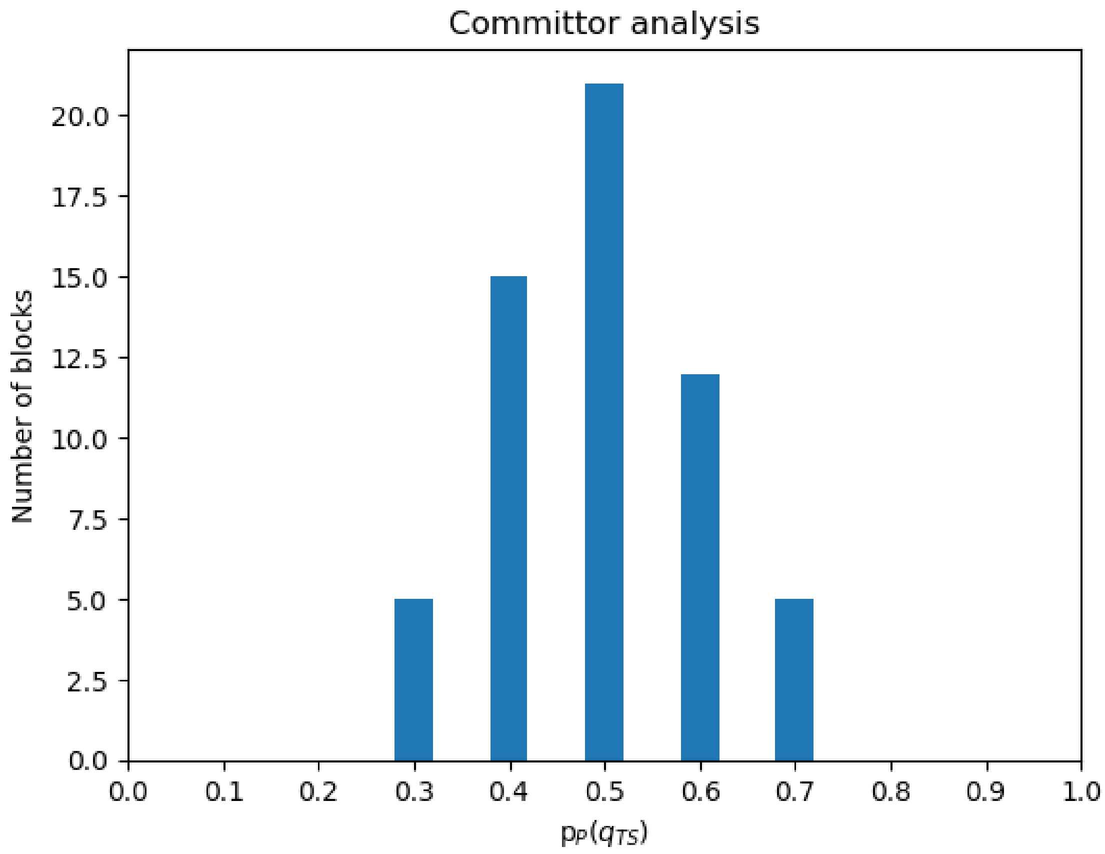

Figure S 17: Committor histogram obtained for the transition state of CV Type CN

13. BIASED MOLECULAR DYNAMICS

When one disposes of a free-energy profile along a specific reaction coordinate q_1, one can easily test the reliability of the energy profile by using the inverse of this profile as bias potential. The resulting free-energy surface should then – in principle - resemble a quasi flat surface. A regular MD simulation on such a surface should sample all regions of the surface with some equal probability. This biased molecular dynamics can be considered as a special type of metadynamics in which the bias potential is provided by the user at the beginning of the simulation and is not updated afterwards.

In case the free-energy barrier is underestimated, the region around the transition state at the global free-energy surface (including the bias potential) will still have an energy which will scarcely to be overcome in a regular MD and thus a low probability is expected that this region will be visited. In case of an overestimation of the energy barrier, the global surface will show some well around the transition state region and an MD simulation will thus sample mainly the region of the TS, and not the reactants and product basins.

We apply this procedure in case of 1D-DI as reaction coordinate. We make use of the F(d_{CM}-d) free-energy profile as extracted in an US protocol. A 14th order polynomial is fitted to the profile (Figure S 18), which is then used as input bias in PLUMED [37] :

$$
\begin{aligned}
w(\xi) = -0.0000329\,\xi^{14} - 0.00146\,\xi^{13} + 0.0246\,\xi^{12} - 0.118\,\xi^{11} + 0.0468\,\xi^{10} + 1.271\,\xi^{9} \\
- 3.185\,\xi^{8} - 2.805\,\xi^{7} + 20.041\,\xi^{6} - 9.635\,\xi^{5} - 56.623\,\xi^{4} + 49.717\,\xi^{3} \\
+ 96.910\,\xi^{2} - 70.297\,\xi^{1} - 118.642
\end{aligned}
$$

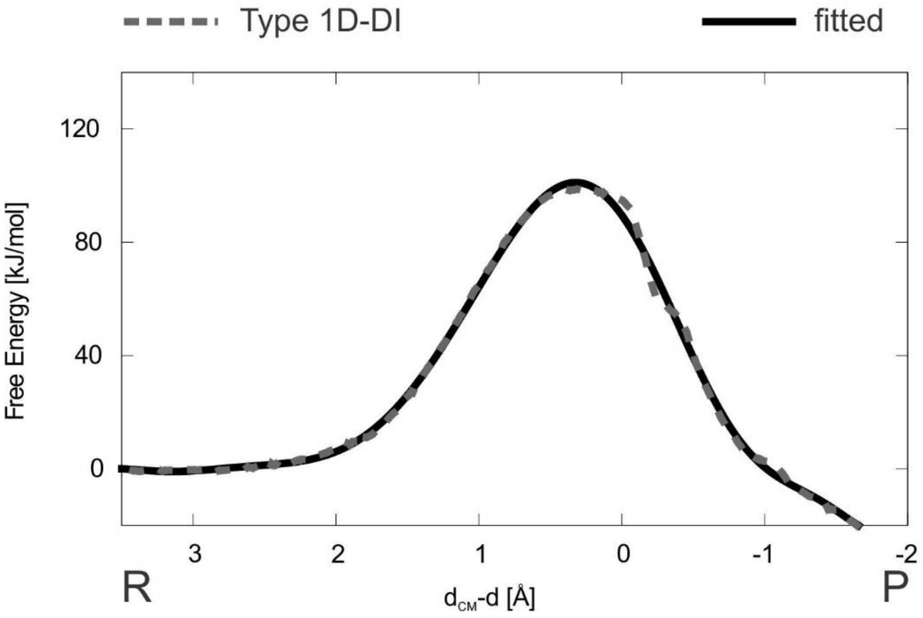

Figure S 18: 14th order polynomial fit to the free energy profile obtained via collective variable 1D-DI and umbrella sampling (US).

As we again are only interested in the forward barrier, the walls used during metadynamics and variationally enhanced sampling are again applied to avoid sampling uninteresting configurations and to increase our efficiency. The histogram of this CV is shown in Figure S 19.

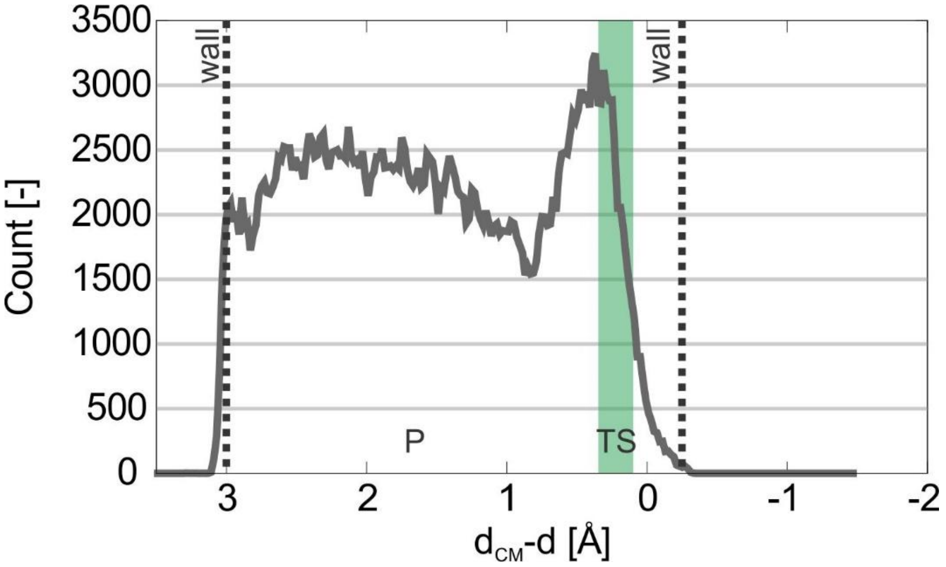

Figure S 19: Histogram of the collective variable 1D-DI for the biased MD simulation.

This plot shows that the collective variable indeed samples the complete reactants basin and transition state region during the biased MD simulation, thus confirming our obtained free energy profile. Nevertheless, the histogram drops significantly after the transition region (d_{CM}-d= 0.1 - 0.35 Å), again confirming the problems we encounter with the product region in the current work. However, the histogram shows that the forward barrier is trustworthy.

14. STATIC RESULTS

As stated in the main manuscript, a direct comparison of our dynamic results with theoretical and experimental data found in literature [38-42] is hampered as they did not report intrinsic free energy barriers or intrinsic reaction rates. There are no generally accepted methodologies to extract enthalpic barriers and adsorption enthalpies directly from ab initio molecular dynamics methods. Two methodologies are proposed to overcome this hurdle.

In a first instance, we also simulated the reactions using periodic DFT calculations in the rigid rotor harmonic oscillator model, to allow a comparison with experimental data and earlier theoretical data. The resulting enthalpy, entropy and free energy data relative to the gas phase for the different steps of the methylation of ethene are summarized in Table S. Furthermore, the static results are compared with available literature data in Table S.

Inspection of the results learns that the obtained adsorption enthalpy for methanol, -99.8 kJ/mol, is very close to the value obtained by Van Speybroeck et al. [42] using cluster calculations, and revealing a slight underestimation of the experimental value of -115 ± 5 kJ/mol. [41, 43] The subsequent co-adsorption enthalpy for ethene attains -13.2 kJ/mol, which is again similar to the -10.35 kJ/mol obtained by Van Speybroeck et al. [42] and underestimating the experimental value varying from -24 and -31 kJ/mol. [41, 44] Finally, the apparent enthalpy barrier amounts to 86.8 kJ/mol, close to the value of Van Speybroeck et al. but 17 kJ/mol lower than the experimental value of 104 kJ/mol. [38-40, 42]

Subsequently, free energy data can be generated from our static results via a post-analysis methodology making use of the in-house developed TAMkin software [45, 46] as applied in recent papers by some of the current authors [5, 9, 47, 48]. This value can be compared with the free energy barrier predicted by the MD simulations. The static intrinsic free energy barrier attains a value of 139.5 kJ/mol, thus overestimating the values obtained via the enhanced sampling methods in this work, as indicated on Figure 5 of the main manuscript.

As no experimental data is available for this free energy barrier, it is difficult to put forward which of the two values is correct.

Secondly, apparent reaction rate constants k_{app} can be obtained from intrinsic reaction rate constants k_{int} by calculating the equilibrium constant for the co-adsorption of ethene, K_1 as follows: [49]

$$CH_3OH\ (ads) + ethene\ (gas) \underset{k_{-1}}{\overset{k_1}{\rightleftharpoons}} CH_3OH\ (ads) + ethene\ (ads) = PRC$$

$$PRC \xrightarrow{k_{int}} Products$$

$$r = k_{int}[PRC]$$

$$\frac{d[PRC]}{dt} = 0 = -k_{int}[PRC] + k_1[ethene(gas)][methanol(ads)] - k_{-1}[PRC]$$

$$r = k_{app}[ethene(gas)][methanol(ads)] = \frac{k_1 \times k_{int}}{k_{-1} + k_{int}}[ethene(gas)][methanol(ads)]$$

$$= K_1\, k_{int}[ethene(gas)][methanol(ads)]$$

$$k_{app} = K_1\, k_{int}$$

where the co-adsorbed methanol and ethene are treated as a pre-reactive complex, PRC. Furthermore, a pseudo-stationary state hypothesis is applied on the PRC and the factor k_{int} in the denominator is assumed to be smaller than k_{-1}, as the reaction is assumed to be kinetically controlled. The equilibrium constant can be calculated from the co-adsorption free energy for ethene $\Delta G_{ads,ethene}$ as:

$$K_1 = V_0 \exp\left(\frac{-\Delta G_{ads,ethene}}{RT}\right)$$

with V_0 the molar volume of an ideal gas at 623 K and 1 atm, equal to 0.0518 m^3/mol.

The relation between intrinsic and apparent rate constants can also easily be derived based on statistical mechanics with the introduction of Gibbs free energies in the determination of reaction rate constants (see Scheme S 1).

(i) The apparent rate constant of the bimolecular reaction:

$$CH_3OH\ (ads) + ethene\ (gas) \rightarrow TS$$

is given by:

$$k_{app} = \frac{k_B T}{h} V_0 \exp(-\frac{\Delta G_{app}}{RT})$$

(ii) The intrinsic rate constant of the monomolecular reaction:

$$PRC \rightarrow TS$$

is given by

$$k_{int} = \frac{k_B T}{h} \exp(-\frac{\Delta G_{int}}{RT})$$

(iii) The equilibrium reaction:

$$CH_3OH\ (ads) + ethene\ (gas) \rightleftharpoons PRC$$

is characterized by its equilibrium constant

$$K_1 = V_0\, exp(-\frac{\Delta G_{ads,ethene}}{RT}) = \frac{k_{+1}}{k_{-1}}$$

Based on the free energy relation $\Delta G_{app} = \Delta G_{ads,ethene} + \Delta G_{int}$, one readily derives $k_{app} = K_1 k_{int}$.

As the co-adsorption free energy $\Delta G_{ads,alkene}$ of alkenes in the MTO process are very functional and dispersion scheme dependent, single point energy calculations are performed with a set of functionals frequently used in literature [47, 50] starting from optimized structures obtained using revPBE-D3. In this work the following set is considered. The revPBE functional can be combined with diverse dispersion schemes. To study their influence, we take several schemes into consideration: D2 corrections, [51] D3 corrections with Becke Johnson damping (BJ), [52] the many body dispersion (MBD) scheme of Tkatchenko-Scheffler, [53] both conventional and with iterative Hirshfeld partitioning (MBD-HI), [54-56] the many body dispersion energy method of Tkatechenko based on the random phase expression for the correlation energy (MBD-rsSCS) [57, 58] and the dDsC dispersion correction. [59, 60] In addition, we also consider multiple functionals of different type: revPBE used as basis for the calculations with vdW-DF of Dion et al. [61, 62], BEEF-vdW, [63] B3LYP-D3 [64] as hybrid functional and SCAN-rVV10. [65] The obtained $\Delta G_{ads,ethene}$ are summarized in Table S. The corresponding equilibrium constants can be found in Table S. The results are discussed in detail in Section 3.4 of the main manuscript.

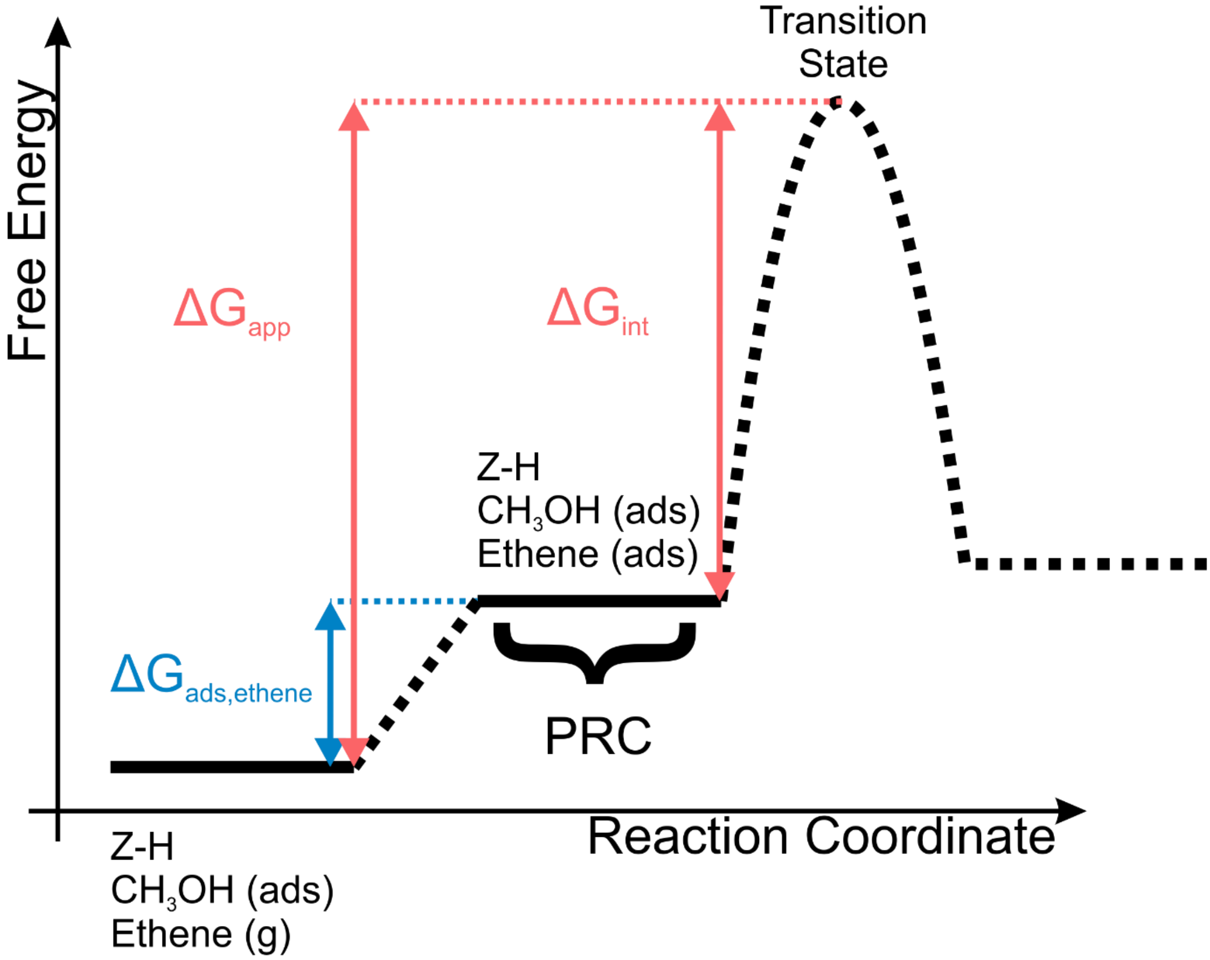

Scheme S 1: Schematic representation of the free energy profile

Table S 9: Enthalpy, entropy and free energy data at 623 K relative to the gas phase for the different steps of the methylation profile of ethene (in kJ/mol).

	CH_3OH (g) Ethene (g) Z-H	CH_3OH (ads) Ethene (g) Z-H	CH_3OH (ads) Ethene (ads) Z-H	Transition State	Product
ΔH	0.0	-99.8	-113.0	-13.0	-129.2
$-T\Delta S$	0.0	93.9	137.2	176.6	160.3
ΔG	0.0	-5.9	24.2	163.6	31.0

Table S 10: Enthalpy values (kJ/mol) from literature and obtained in the current paper of the various steps for the methylation of ethene at 623 K (unless stated otherwise).

	Experimental	Svelle et al. [41]	Van Speybroeck et al. [42]	Piccini et al. [38]	Current paper
$\Delta H_{ads,methanol}$	-115±5[a] [26,28]	-115[c]	-97.3[e]	n.a.	-99.8
$\Delta H_{co-ads,ethene}$	-24 - -31[b] [26,29]	-37[c]	1.6 (-10.4[e])	n.a.	-13.2
$\Delta H^{\neq}_{app}$	104 [24,25]	104	83.2	105.4	86.8
$\Delta H^{\neq}_{int}$	n.a.	119[d]	84.03[e]	n.a.	100.0

[a] Only available at 400 K. [b] Only available in the range 298 – 353 K [c] Only electronic energies (0 K) with PBE-D available for these values in re .[41]. [d] Only electronic energies (0 K) with PBE available for these values in SI of ref [41]. [e] Only electronic energies with ONIOM(B3LYP/6-31+g(d):HF/6-31+g(d)) level of theory with inclusion of van der Waals corrections for these values in ref [42].

Table S 11: Adsorption energy and free energy for the co-adsorption of ethene using various functionals and dispersion corrections schemes (kJ/mol).

	revPBE-D3	revPBE-D2	revPBE-D3(BJ)	revPBE-MBD	revPBE-MBD_HI	revPBE-MBD_rSC	revPBE-DdSc	BEEF_vdW	vdW-DF of Dion	B3LYP-D3	SCAN-rVV10
$\Delta E_{ads,ethene}$	-22.7	-12.0	-22.0	-21.3	-18.7	-12.0	-11.0	-23.6	-36.8	-20.3	-11.9
$\Delta G_{ads,ethene}$	30.1	40.8	30.8	31.5	34.1	40.8	41.7	29.1	16.0	32.5	40.9

Table S 12: Equilibrium constants for the co-adsorption of ethene using various functionals and dispersion correction schemes (m^3/mol).

	revPBE-D3	revPBE-D2	revPBE-D3(BJ)	revPBE-MBD	revPBE-MBD_HI	revPBE-MBD_rSC	revPBE-DdSc	BEEF_vdW	vdW-DF of Dion	B3LYP-D3	SCAN-rVV10
K_1	1.57 10^{-4}	1.96 10^{-5}	1.36 10^{-4}	1.18 10^{-4}	7.19 10^{-5}	1.96 10^{-5}	1.64 10^{-5}	1.87 10^{-4}	2.35 10^{-3}	9.75 10^{-5}	1.94 10^{-5}

REFERENCES

[1] J. Dědeček, S. Sklenak, C. Li, B. Wichterlová, V. Gábová, J. Brus, M. Sierka, J. Sauer, Aluminum Siting in the Framework of Silicon Rich Zeolites. A ZSM-5 Study., in: Zeolites and related materials: Trends, targets and challenges, Elsevier, 2008, pp. 781-786.
[2] J. Van der Mynsbrugge, K. Hemelsoet, M. Vandichel, M. Waroquier, V. Van Speybroeck, Efficient Approach for the Computational Study of Alcohol and Nitrile Adsorption in H-ZSM-5, J. Phys. Chem. C, 116 (2012) 5499-5508.
[3] A. Bhan, Y.V. Joshi, W.N. Delgass, K.T. Thomson, DFT investigation of alkoxide formation from olefins in H-ZSM-5, Journal of Physical Chemistry B, 107 (2003) 10476-10487.
[4] I. Yarulina, S. Bailleul, A. Pustovarenko, J.R. Martinez, K. De Wispelaere, J. Hajek, B.M. Weckhuysen, K. Houben, M. Baldus, V. Van Speybroeck, F. Kapteijn, J. Gascon, Suppression of the Aromatic Cycle in Methanol-to-Olefins Reaction over ZSM-5 by Post-Synthetic Modification Using Calcium, Chemcatchem, 8 (2016) 3057-3063.
[5] I. Yarulina, K. De Wispelaere, S. Bailleul, J. Goetze, M. Radersma, E. Abou-Hamad, I. Vollmer, M. Goesten, B. Mezari, E.J.M. Hensen, J.S. Martinez-Espin, M. Morten, S. Mitchell, J. Perez-Ramirez, U. Olsbye, B.M. Weckhuysen, V. Van Speybroeck, F. Kapteijn, J. Gascon, Structure-performance descriptors and the role of Lewis acidity in the methanol-to-propylene process, Nat. Chem., 10 (2018) 804-812.
[6] K. De Wispelaere, S. Bailleul, V. Van Speybroeck, Towards molecular control of elementary reactions in zeolite catalysis by advanced molecular simulations mimicking operating conditions, Catalysis Science & Technology, 6 (2016) 2686-2705.
[7] S. Bailleul, S.M.J. Rogge, L. Vanduyfhuys, V. Van Speybroeck, Insight into the Role of Water on the Methylation of Hexamethylbenzene in H-SAPO-34 from First Principle Molecular Dynamics Simulations, Chemcatchem, 11 (2019) 3993-4010.
[8] S. Bailleul, I. Yarulina, A.E.J. Hoffman, A. Dokania, E. Abou-Hamad, A.D. Chowdhury, G. Pieters, J. Hajek, K. De Wispelaere, M. Waroquier, J. Gascon, V. Van Speybroeck, A Supramolecular View on the Cooperative Role of Bronsted and Lewis Acid Sites in Zeolites for Methanol Conversion, Journal of the American Chemical Society, 141 (2019) 14823-14842.
[9] P. Cnudde, K. De Wispelaere, J. Van der Mynsbrugge, M. Waroquier, V. Van Speybroeck, Effect of temperature and branching on the nature and stability of alkene cracking intermediates in H-ZSM-5, Journal of Catalysis, 345 (2017) 53-69.
[10] R. Demuynck, S.M.J. Rogge, L. Vanduyfhuys, J. Wieme, M. Waroquier, V. Van Speybroeck, Efficient Construction of Free Energy Profiles of Breathing Metal-Organic Frameworks Using Advanced Molecular Dynamics Simulations, Journal of Chemical Theory and Computation, 13 (2017) 5861-5873.
[11] B. Peters, Reaction Coordinates and Mechanistic Hypothesis Tests, in: M.A. Johnson, T.J. Martinez (Eds.) Annual Review of Physical Chemistry, Vol 67, 2016, pp. 669-690.
[12] T. Bucko, Ab initio calculations of free-energy reaction barriers, Journal of Physics-Condensed Matter, 20 (2008) 064211.
[13] A. Laio, M. Parrinello, Escaping free-energy minima, Proceedings of the National Academy of Sciences of the United States of America, 99 (2002) 12562-12566.
[14] M. Iannuzzi, A. Laio, M. Parrinello, Efficient exploration of reactive potential energy surfaces using Car-Parrinello molecular dynamics, Phys. Rev. Lett., 90 (2003) 4.
[15] O. Valsson, M. Parrinello, Variational Approach to Enhanced Sampling and Free Energy Calculations, Phys. Rev. Lett., 113 (2014).
[16] F. Bach, E. Moulines, Non-strongly-Convex Smooth Stochastic Approximation with Convergence Rate O(1/n), in: C.J.C. Burges, Bottou, L., Welling, M., Ghahramani, Z., Weinberger, K.Q. (Ed.) Advances in Neural Information Processing Systems 26, Curran Associates , Inc., 2013, pp. 773-781.

[17] M. Souaille, B. Roux, Extension to the weighted histogram analysis method: combining umbrella sampling with free energy calculations, Computer Physics Communications, 135 (2001) 40-57.
[18] S. Kumar, D. Bouzida, R.H. Swendsen, P.A. Kollman, J.M. Rosenberg, THE WEIGHTED HISTOGRAM ANALYSIS METHOD FOR FREE-ENERGY CALCULATIONS ON BIOMOLECULES .1. THE METHOD, Journal of Computational Chemistry, 13 (1992) 1011-1021.
[19] J. Kastner, W. Thiel, Bridging the gap between thermodynamic integration and umbrella sampling provides a novel analysis method: "umbrella integration", Journal of Chemical Physics, 123 (2005).
[20] G.M. Torrie, J.P. Valleau, NON-PHYSICAL SAMPLING DISTRIBUTIONS IN MONTE-CARLO FREE-ENERGY ESTIMATION - UMBRELLA SAMPLING, Journal of Computational Physics, 23 (1977) 187-199.
[21] P. Cnudde, K. De Wispelaere, L. Vanduyfhuys, R. Demuynck, J. Van der Mynsbrugge, M. Waroquier, V. Van Speybroeck, How Chain Length and Branching Influence the Alkene Cracking Reactivity on H-ZSM-5, Acs Catalysis, 8 (2018) 9579-9595.
[22] J. Hajek, C. Caratelli, R. Demuynck, K. De Wispelaere, L. Vanduyfhuys, M. Waroquier, V. Van Speybroeck, On the intrinsic dynamic nature of the rigid UiO-66 metal-organic framework, Chem. Sci., 9 (2018) 2723-2732.
[23] F.Q. Zhu, G. Hummer, Convergence and error estimation in free energy calculations using the weighted histogram analysis method, Journal of Computational Chemistry, 33 (2012) 453-465.
[24] H. Grubmuller, B. Heymann, P. Tavan, Ligand binding: Molecular mechanics calculation of the streptavidin biotin rupture force, Science, 271 (1996) 997-999.
[25] J. Kastner, Umbrella sampling, Wiley Interdisciplinary Reviews-Computational Molecular Science, 1 (2011) 932-942.
[26] J. Kastner, W. Thiel, Analysis of the statistical error in umbrella sampling simulations by umbrella integration, Journal of Chemical Physics, 124 (2006).
[27] D. Frenkel, B. Smit, Understanding Molecular Simulation, second edition ed., Academic press, Elsevier, 2002.
[28] P. Hanggi, P. Talkner, M. Borkovec, REACTION-RATE THEORY - 50 YEARS AFTER KRAMERS, Reviews of Modern Physics, 62 (1990) 251-341.
[29] T. Bucko, S. Chibani, J.F. Paul, L. Cantrel, M. Badawi, Dissociative iodomethane adsorption on Ag-MOR and the formation of Agl clusters: an &ITab initio&IT molecular dynamics study, Physical Chemistry Chemical Physics, 19 (2017) 27530-27543.
[30] G. Ciccotti, M. Ferrario, Blue moon approach to rare events, Molecular Simulation, 30 (2004) 787-793.
[31] B.J. Berne, M. Borkovec, J.E. Straub, CLASSICAL AND MODERN METHODS IN REACTION-RATE THEORY, J. Phys. Chem., 92 (1988) 3711-3725.
[32] E.A. Carter, G. Ciccotti, J.T. Hynes, R. Kapral, CONSTRAINED REACTION COORDINATE DYNAMICS FOR THE SIMULATION OF RARE EVENTS, Chemical Physics Letters, 156 (1989) 472-477.
[33] P.W. Atkins, Physical Chemistry, Oxford.
[34] R. Demuynck, J. Wieme, S.M.J. Rogge, K.D. Dedecker, L. Vanduyfhuys, M. Waroquier, V. Van Speybroeck, Protocol for Identifying Accurate Collective Variables in Enhanced Molecular Dynamics Simulations for the Description of Structural Transformations in Flexible Metal-Organic Frameworks, Journal of Chemical Theory and Computation, 14 (2018) 5511-5526.
[35] G. Perez-Hernandez, F. Paul, T. Giorgino, G. De Fabritiis, F. Noe, Identification of slow molecular order parameters for Markov model construction, Journal of Chemical Physics, 139 (2013).
[36] C.R. Schwantes, V.S. Pande, Improvements in Markov State Model Construction Reveal Many Non-Native Interactions in the Folding of NTL9, Journal of Chemical Theory and Computation, 9 (2013) 2000-2009.
[37] M. Bonomi, D. Branduardi, G. Bussi, C. Camilloni, D. Provasi, P. Raiteri, D. Donadio, F. Marinelli, F. Pietrucci, R.A. Broglia, M. Parrinello, PLUMED: A portable plugin for free-energy

calculations with molecular dynamics, Computer Physics Communications, 180 (2009) 1961-1972.
[38] G. Piccini, M. Alessio, J. Sauer, AbInitio Calculation of Rate Constants for Molecule-Surface Reactions with Chemical Accuracy, Angewandte Chemie-International Edition, 55 (2016) 5235-5237.
[39] S. Svelle, P.A. Ronning, S. Kolboe, Kinetic studies of zeolite-catalyzed methylation reactions 1. Coreaction of [C-12]ethene and [C-13]methanol, Journal of Catalysis, 224 (2004) 115-123.
[40] S. Svelle, P.O. Ronning, U. Olsbye, S. Kolboe, Kinetic studies of zeolite-catalyzed methylation reactions. Part 2. Co-reaction of [C-12]propene or [C-12]n-butene and [C-13]methanol, Journal of Catalysis, 234 (2005) 385-400.
[41] S. Svelle, C. Tuma, X. Rozanska, T. Kerber, J. Sauer, Quantum Chemical Modeling of Zeolite-Catalyzed Methylation Reactions: Toward Chemical Accuracy for Barriers, Journal of the American Chemical Society, 131 (2009) 816-825.
[42] V. Van Speybroeck, J. Van der Mynsbrugge, M. Vandichel, K. Hemelsoet, D. Lesthaeghe, A. Ghysels, G.B. Marin, M. Waroquier, First Principle Kinetic Studies of Zeolite-Catalyzed Methylation Reactions, Journal of the American Chemical Society, 133 (2011) 888-899.
[43] C.C. Lee, R.J. Gorte, W.E. Farneth, Calorimetric study of alcohol and nitrile adsorption complexes in H-ZSM-5, Journal of Physical Chemistry B, 101 (1997) 3811-3817.
[44] S. Jakobtorweihen, N. Hansen, F.J. Keil, Molecular simulation of alkene adsorption in zeolites, Molecular Physics, 103 (2005) 471-489.
[45] B.A. De Moor, A. Ghysels, M.-F. Reyniers, V. Van Speybroeck, M. Waroquier, G.B. Marin, Normal Mode Analysis in Zeolites: Toward an Efficient Calculation of Adsorption Entropies, Journal of Chemical Theory and Computation, 7 (2011) 1090-1101.
[46] A. Ghysels, T. Verstraelen, K. Hemelsoet, M. Waroquier, V. Van Speybroeck, TAMkin: A Versatile Package for Vibrational Analysis and Chemical Kinetics, Journal of Chemical Information and Modeling, 50 (2010) 1736-1750.
[47] J. Hajek, B. Bueken, M. Waroquier, D. De Vos, V. Van Speybroeck, The Remarkable Amphoteric Nature of Defective UiO-66 in Catalytic Reactions, Chemcatchem, 9 (2017) 2203-2210.
[48] J. Hajek, J. Van der Mynsbrugge, K. De Wispelaere, P. Cnudde, L. Vanduyfhuys, M. Waroquier, V. Van Speybroeck, On the stability and nature of adsorbed pentene in Bronsted acid zeolite H-ZSM-5 at 323 K, Journal of Catalysis, 340 (2016) 227-235.
[49] B. De Sterck, R. Vaneerdeweg, F. Du Prez, M. Waroquier, V. Van Speybroeck, Solvent Effects on Free Radical Polymerization Reactions: The Influence of Water on the Propagation Rate of Acrylamide and Methacrylamide, Macromolecules, 43 (2010) 827-836.
[50] J. Wieme, K. Lejaeghere, G. Kresse, V. Van Speybroeck, Tuning the balance between dispersion and entropy to design temperature-responsive flexible metal-organic frameworks, Nat. Commun., 9 (2018).
[51] S. Grimme, Semiempirical GGA-type density functional constructed with a long-range dispersion correction, Journal of Computational Chemistry, 27 (2006) 1787-1799.
[52] S. Grimme, S. Ehrlich, L. Goerigk, Effect of the Damping Function in Dispersion Corrected Density Functional Theory, Journal of Computational Chemistry, 32 (2011) 1456-1465.
[53] A. Tkatchenko, M. Scheffler, Accurate Molecular Van Der Waals Interactions from Ground-State Electron Density and Free-Atom Reference Data, Phys. Rev. Lett., 102 (2009) 073005.
[54] T. Bucko, S. Lebegue, J.G. Angyan, J. Hafner, Extending the applicability of the Tkatchenko-Scheffler dispersion correction via iterative Hirshfeld partitioning, Journal of Chemical Physics, 141 (2014).
[55] T. Bucko, S. Lebegue, J. Hafner, J.G. Angyan, Improved Density Dependent Correction for the Description of London Dispersion Forces, Journal of Chemical Theory and Computation, 9 (2013) 4293-4299.
[56] P. Bultinck, C. Van Alsenoy, P.W. Ayers, R. Carbo-Dorca, Critical analysis and extension of the Hirshfeld atoms in molecules, Journal of Chemical Physics, 126 (2007) 144111.
[57] A. Ambrosetti, A.M. Reilly, R.A. DiStasio, Jr., A. Tkatchenko, Long-range correlation energy calculated from coupled atomic response functions, Journal of Chemical Physics, 140 (2014).

[58] A. Tkatchenko, R.A. DiStasio, Jr., R. Car, M. Scheffler, Accurate and Efficient Method for Many-Body van der Waals Interactions, Phys. Rev. Lett., 108 (2012).
[59] S.N. Steinmann, C. Corminboeuf, Comprehensive Bench marking of a Density-Dependent Dispersion Correction, Journal of Chemical Theory and Computation, 7 (2011) 3567-3577.
[60] S.N. Steinmann, C. Corminboeuf, A generalized-gradient approximation exchange hole model for dispersion coefficients, Journal of Chemical Physics, 134 (2011).
[61] M. Dion, H. Rydberg, E. Schroder, D.C. Langreth, B.I. Lundqvist, Van der Waals density functional for general geometries, Phys. Rev. Lett., 92 (2004) 246401.
[62] J. Klimes, D.R. Bowler, A. Michaelides, Van der Waals density functionals applied to solids, Physical Review B, 83 (2011).
[63] J. Wellendorff, K.T. Lundgaard, A. Mogelhoj, V. Petzold, D.D. Landis, J.K. Norskov, T. Bligaard, K.W. Jacobsen, Density functionals for surface science: Exchange-correlation model development with Bayesian error estimation, Physical Review B, 85 (2012) 235149.
[64] A.D. Becke, DENSITY-FUNCTIONAL THERMOCHEMISTRY .3. THE ROLE OF EXACT EXCHANGE, Journal of Chemical Physics, 98 (1993) 5648-5652.
[65] H.W. Peng, Z.H. Yang, J.P. Perdew, J.W. Sun, Versatile van der Waals Density Functional Based on a Meta-Generalized Gradient Approximation, Physical Review X, 6 (2016).